Tracking the summit activity of Mt. Etna volcano between July 2019 and January 2020 by integrating petrological and geophysical data

Marisa Giuffrida[1], Mariabenedetta Scandura[1], Giorgio Costa[1], Francesco Zuccarello[1], Mariangela Sciotto[2], Andrea Cannata[1,2], Marco Viccaro[1,2*]

[1] *Università degli Studi di Catania, Dipartimento di Scienze Biologiche, Geologiche e Ambientali, Corso Italia 57, I-95129, Catania, Italy*

[2] *Istituto Nazionale di Geofisica e Vulcanologia – Sezione di Catania, Osservatorio Etneo, Piazza Roma 2, I-95125 Catania, Italy*

* Corresponding author: phone +39 0957195741; e-mail: m.viccaro@unict.it

Abstract

The evolution of volcanic activity observed at the New South East Crater (NSEC) and Voragine (VOR) between July 2019 and January 2020 has been deciphered by taking into account the changes of textures and chemical zoning of plagioclase and olivine crystals from the erupted lavas and tephra. The petrological observations have been integrated with analyses of the amplitude and source location of volcanic tremor and infrasound data. Characteristics of crystals erupted on July 2019 at the NSEC reflect protracted intrusions of magma into the mid-upper section of the plumbing system, approximately within 290-120 MPa, which acted as the main zone of magma accumulation and crystallization before the beginning of the eruptive activity. Textures and compositions of crystals erupted at VOR emphasize the beginning of volcanic activity driven by recharge/discharge phases that mostly affect the shallowest portion of the Mt. Etna plumbing system (<40 MPa). At the end of 2019, mineral compositions and zoning patterns changed again in accordance with eruption dynamics. The observed changes reflect the transition from an early phase, between November and December 2019, characterized by substantial equilibrium during magma storage and transport towards higher disequilibrium conditions and eruptive frequency, in January 2020. This has been associated to episodes of deep replenishment of mafic magmas displacing the resident one. Diffusion chronometry applied to zoned olivines shows that most of the episodes of magma intrusion correlate temporally with changes in the features of both volcanic tremor and infrasonic events in terms of amplitude and source location, providing evidence that such geophysical signals are directly related to the magma dynamics in the upper plumbing system.

Keywords: Mt. Etna; plagioclase textures; olivine zoning; diffusion modeling; volcanic tremor; infrasound.

1. Introduction

Mt. Etna is acknowledged for the persistent and highly variable eruptive activity from both the summit craters and the volcano flanks. Eruptions at the summit often involve more than one crater at a time and can last from a few hours to several months, evolving by phases of degassing alternating with Strombolian activity and lava overflows and, occasionally, paroxysms and lava fountains (e.g., Del Carlo and Pompilio, 2004; Branca and Del Carlo, 2005; Harris et al., 2011). The last decade has seen the New South East Crater (NSEC) as the principal site of the eruptive activity. After a three-year-long sequence of paroxysmal eruptions and lava fountaining (e.g., 2011-2013; Behncke et al., 2014; Spampinato et al., 2015; Giuffrida and Viccaro, 2017), the activity at NSEC has been characterized by intermittent Strombolian explosions of variable intensity and lava effusions (e.g., 2014-2015), becoming increasingly more effusive in the following years (e.g., February-April 2017 and December 2018). Aside from NSEC, only the crater Voragine (VOR) recently produced major eruptive episodes, while the other summit vents Bocca Nuova (BN), North East Crater (NEC) and South East Crater (SEC) have been less involved. Violent paroxysms originated at VOR on December 2015 and May 2016, with explosions producing significant morphological changes in the volcano summit, along with changes in the modes of magma storage and transfer in the upper plumbing system (Corsaro et al., 2017; Pompilio et al., 2017; Cannata et al., 2018; Calvari et al., 2018; Viccaro et al., 2019).

The summit activity throughout 2019 and 2020 has seen four of the five summit craters intermittently active, although the most interesting feature is probably the resumption of volcanic activity at VOR after more than three years since the powerful episodes of 2015-2016. The eruptive phenomena of 2019-2020 have been highly variable, with overall Strombolian explosions of different intensity from all the summit craters, punctuated by lava flows from NSEC in May and July 2019 and from VOR toward the end of 2019 (**Fig. 1**).

Our ability to monitor volcanoes using data coming from distinct types of observations (e.g., petrological data, seismic and infrasonic signals, measurements of ground deformation, gravity and magnetic data, gas flux, satellite imagery) has dramatically increased in recent years, and they contributed to produce advanced models of volcanic processes (e.g., Aiuppa et al., 2007, 2010a, 2010b; Martí et al., 2013; Patanè et al., 2013). Despite the continuous advances, the complexity of interpreting multiple monitoring data often plays in favor of a monodisciplinary investigation that typically explore a specific aspect of the volcano dynamics, while potentially hiding other more complex internal processes.

Regular sampling and petrological analysis of the erupted products (lavas, tephra and their crystal cargo) represent a valuable approach for monitoring short- to long-term changes of the plumbing

system of active and dormant volcanoes (Luhr and Carmichael, 1990; Corsaro and Miraglia, 2005; Francalanci et al., 2012; Viccaro et al., 2016a; Giuffrida et al., 2018, 2020; Mangler et al., 2019, 2020; Zuccarello et al., 2021). A higher resolution in detecting magma dynamics derives from analyses of textures and chemical zonation of magmatic crystals, whose core-to-rim record reflects progressive thermodynamic changes of the magma in which they grew (e.g., Loomis, 1983; Kohn et al., 1989; Cashman, 1990; Davidson and Tepley, 1997; Stewart and Fawler, 2001; Wallace and Bergantz, 2002; Ruprecht and Worner, 2007; Streck, 2008; Kahl et al., 2011, 2013, 2015, 2017). In fact, the systematic analysis and correlation between zoned crystals coming from distinct, subsequent eruptions have proved to be particularly effective to detect temporal changes of the conditions of storage, transfer and interaction of magmas through distinct sections of volcano plumbing systems (Kahl et al., 2011, 2013, 2015; Druitt et al., 2012; Viccaro et al., 2012, 2016b; Lynn et al., 2017; Gordeychic et al., 2018; Di Stefano et al., 2020; Giuffrida et al., 2020; Mangler et al., 2020). Such petrological approaches have been also successfully applied in combination with real-time geophysical monitoring signals to unravel the sequence of magmatic events through complex networks worldwide (Saunders et al., 2012; Martí et al., 2013; Pankhurst et al., 2014; 2018; Viccaro et al., 2016b, 2021; Mutch et al., 2019), including the present-day plumbing system of Mt. Etna (Kahl et al., 2011, 2013, 2015; Viccaro et al., 2014, 2016c, 2019; Palano et al., 2017; Cannata et al., 2018; Borzì et al., 2020).

The 2019 reawakening of VOR, after years of volcanic activity dominated by the NSEC eruptions, poses the challenge to clarify the conditions that drive magmas towards different eruptive vents and therefore, develop a better understanding of the existing connection among magma pathways beneath Mt. Etna volcano. In order to reconstruct the conditions of magma accumulation, ascent and recharge prior to the eruption, we present in this work an overview of Mt. Etna eruptions at NSEC and VOR from mid-2019 to early 2020, focusing on textures and zoning of plagioclase and olivine crystals. The chemical diffusion in olivine has been used as a proxy to estimate the time at which such processes have occurred. The petrological data and interpretations have also been integrated with results of time-series analysis and source location of real-time volcanic tremor and infrasound data. All the available data have been finally correlated with volcanological observations in order to get insights into the existing relationships between modes of magma supply and changes in the state of volcanic activity at the surface.

This study builds upon and pursues the existing studies and results on Mt. Etna plumbing system dynamics and storage conditions observed in the last decade from a crystal chemistry plus geophysical perspective. The sequence of magmatic events of 2019-2020 is interpreted within the framework of the most recent activity of Mt. Etna with the aim to illustrate how the volcano plumbing system works to date. We put into attention the short-term variability in storage conditions and ascent dynamics that has been recognized as the engine for past eruptions (Patanè et al., 2013; Kahl et al.,

2011, 2013, 2015; Bonforte et al., 2017; Giuffrida and Viccaro, 2017, Cannata et al., 2018; Ubide and Kamber, 2018). Special emphasis is given to the post-2017 events that were precursory to the onset of the new eruptive phase on May 2019 (Viccaro et al., 2019; Borzì et al., 2020). Considerations on the recent eruptive record are used to test the recurrence of magmatic conditions and processes that may have caused changes in the current state of volcanic activity.

2. Chronology of the 2019-2020 eruptive episodes

The reactivation of VOR on September 12, 2019 was preceded by a period of intensification of the volcanic activity at NEC, BN and NSEC **(Fig. 1a)**. During the first months of the 2019, NEC and BN displayed continuous degassing and sporadic ash emission. On May 30, 2019 two fracture systems opened and propagated along the southeastern and northern flanks of the NSEC, generating weak Strombolian explosions and lava overflows (**Fig. 1b)**. The emission of lavas progressively decreased during the following days, and finally stopped on June 5. On the second half of July, two further eruptive episodes occurred at NSEC, the first on July 18-20 and the second on July 27-28 (**Fig. 1b**). Both episodes displayed similar eruptive dynamics, producing Strombolian explosions from the summit vent and lava flows from eruptive fractures located on the northern and southern side of the cone, respectively. In particular, the latter episode differs from the former for a sequence of intense explosions that lasted for hours and produced an ash column rising up to 7.5 km a.s.l. (INGV-OE Internal Report, 2019a). The eruptions of July were followed by a period of intense degassing at NSEC, NEC and BN. On September 8, Strombolian activity began at NEC, continuing with variable intensity during the following days, together with diffuse ash emission (**Fig. 1b**).

The crater VOR awoke again in the morning of September 12 with ash puffs that increased gradually in frequency until turning into mild-to-high intensity Strombolian explosions. In mid-September, a scoria cone started forming on the crater floor, and continued to grow during the following months due to the abundant tephra fallout around the active vent. The activity at VOR persisted for the next eight months, but it was highly variable in intensity (**Fig. 1b**). Peaks at highest eruptive intensity were observed in November 2019 and in the period January-February 2020 (INGV-OE Internal Report, 2019b, 2019c, 2020a, 2020b). During such periods of intense explosions, small lava flows were emitted from the scoria cone into the adjacent BN crater (insert in **Fig. 1a**).

On mid-April 2020, the main site of Strombolian activity involved again the NSEC, whereas NEC and BN only produced sporadic ash puffs or weak Strombolian explosions (**Fig. 1b**).

3. Petrological results

3.1 Sampling and analytical methods

Fourteen lava and tephra samples were taken at the summit areas of Mt. Etna during some eruptive phases encompassing the volcanic activity between July 2019 and January 2020. Specifically, seven samples are lava rocks collected ~2 km far from the NSEC, right at the front of the active lava flow field of July 27-28 (**Fig. 1a**). Additional seven samples refer to the activity at the crater VOR throughout the period November 2019 - January 2020. They are scoria collected close to the eastern and western side of the crater edge on November 4, 2019, December 19-20, 2019 and on January 24, 2020, when the eruption was still in progress.

Samples were inspected on polished thin sections under optical and electron microscopy. Mineral textures and compositions were studied using back-scattered electron images (BSE; 1024×864 pixels) and scanning electron microscopy at the Dipartimento di Scienze Biologiche, Geologiche e Ambientali of the University of Catania, Italy. Major element abundances were measured along core-to-rim traverses for a selection of plagioclase (39 crystals; **Supplementary Material 1**) and olivine (45 crystals; **Supplementary Material 2**). Analytical traverses were done parallel to the longest side, crosscutting the center of plagioclase and olivine, with spacing between individual spots of 4-10 μm depending on the crystal size. Single analytical spots were acquired for the compositional characterization of clinopyroxene and opaque oxides. Microanalytical data were acquired with a Tescan Vega-LMU scanning electron microscope (SEM) equipped with an EDAX Neptune XM4-60 micro-analyzer operating by energy dispersive system (EDS). The microscope is equipped with an ultra-thin Be window, and it is coupled with an EDAX WDS LEXS (wavelength dispersive low energy x-ray spectrometer) calibrated for light elements. Instrumentation and operating conditions to obtain high-contrast BSE image and the analysis of major elements were set at 20 kV accelerating voltage and 2 nA beam current. Repeated analyses were performed on internationally certified minerals and glass standards during the analytical runs. Under the reported analytical conditions, precision is on the order of 3-5% for all the collected elements, while the accuracy is around 5%.

3.2 Diffusion modeling procedure

We modeled the diffusive relaxation of 20 profiles in zoned olivine in an attempt to extract the timescales of magmatic processes drawn out from the examination of olivine composition and types of zoning. The modeling was performed numerically with the method of finite differences (Costa et al., 2008) considering isothermal diffusion and constant boundary conditions.

We accounted for diffusion anisotropy by determining the olivine a-, b- and c- crystallographic axes and the angles between the SEM-EDS/WDS traverses and the three axes. Crystallographic axes were measured by conoscopic observations under a polarizing optical microscope equipped with a Zeiss 4 axis universal stage. We plotted the data onto a lower hemisphere stereographic projection and measured the angle between the orientation of axes and the analytical traverse. The α, β and γ

angles between the traverse and the crystallographic axes of the olivine were finally used to calculate appropriated Fe-Mg diffusion coefficients ($D_{Fe\text{-}Mg}$; Dohmen and Chakraborty, 2007) for modeling the zoning profiles. Concentration profiles obtained from randomly sectioned olivine crystals were not modeled. Typically, the largest errors result from modeling profiles in sections that are oblique to crystal faces. Off-center sections intersect crystal faces at very different angles, thus generating apparent concentration gradients of different widths (Wallace and Bergantz, 2003). We have used simple guidelines suggested in many studies (e.g., Costa and Chakraborty 2004; Costa et al., 2008; Shea et al., 2015a, 2015b) to select the best sectioned crystals among the numerous olivines exposed in thin sections. For instance, we have selected only sections cutting the crystal close to the fastest diffusion direction (i.e., the c-axis; Costa and Chakraborty 2004). Moreover, we disregard the smallest olivines, which have high probability of being off-center sections of olivine. Composition-dependent diffusion coefficients were determined for any observed olivine population by using the thermodynamic parameters (T, P, and fO_2) that define a physical environment consistent with the array of crystallization conditions recognized at Mt. Etna for the post-2011 activity (Giuffrida and Viccaro, 2017). Uncertainties on diffusion timescales were obtained by propagating the error in the determination of diffusion coefficients $D_{Fe\text{-}Mg}$. The procedure for the error propagation analysis follows criteria introduced by Kahl et al. (2015) and accounts for changes in temperature and oxygen fugacity associated to any observed olivine population. We assumed uncertainties of ±10°C on temperature and ±0.25 log fO_2, where fO_2 is in bars, on the basis of thermodynamic conditions of crystallization fixed for magmatic environments at Mt. Etna (Giuffrida and Viccaro, 2017). Note that the adopted temperature range is large enough to include the systematic uncertainties associate with thermodynamics simulations (cf. Giuffrida and Viccaro, 2017 for details).

The diffusion model parameters and results are provided in **Table 1** and **Supplementary Material 3**. We obtained 20 independent time estimates from modeling of olivine zoning.

Ten of the modeled crystals exhibited simple normal (N) or reverse (R) zoning, which has been modeled with a single timescale. The other crystals exhibit complex zoning, R+N or N+R. Timescales for these crystals were calculated only for the interior zone because the chemical gradient rimward is recorded by just few analytical spots or it was too small (~1 Fo mol%) to be modeled. In two crystals, complex zoning was modeled in separate steps, one for the interior zone and the other for the rim.

A step-like distribution has been applied as the initial concentration ~~profile~~ to model both normal and reverse zoning patterns. This choice follows the reasoning that the zoning is created abruptly by magma recharge or rapid intrusion into a compositional-distinct reservoir. All timescales are referred to as 'maximum' due to the assumption that the final Fe-Mg zoning has originated by diffusion only. The potential contribution of crystal growth versus diffusion has been not resolved because of the inability to discern between the effect of concurrent diffusion and growth without relying on minor

elements diffusing at different rates (Shea et al., 2015a, 2015b; Oeser et al., 2018). Assuming a diffusion only contribution, the modeling yields timescales that might be longer than those obtained by fitting a profile derived by a diffusion plus growth model (Costa et al., 2008). However, the advantage of using such simplified approach in an articulated plumbing system like Mt. Etna is that it allows simplifying complex magmatic dynamics that likely involves non-isothermal diffusion and moving boundary conditions during the transfer of the crystal from a magmatic environment to another. Here, we assumed that diffusion started as the crystal is incorporated in a magmatic environment having thermodynamic characteristics quite different than the initial conditions, and that the new conditions were able to produce abrupt compositional changes (i.e., step-like initial profile) in the crystal involved. Thus, the choice of isothermal diffusion accounts for a mechanism of chemical relaxation of a given olivine at the temperature of the final host environment (**Table 1**).

The reliability of the modeling relies on the fact that diffusion curves fit particularly well the measured profiles without invoking changes in temperature and boundary conditions with time. Also, retrieved timescales of olivine residence and re-equilibration in our dataset are fully consistent with those recovered from recent eruptions at Mt. Etna (Kahl et al., 2011, 2013, 2015; Giuffrida and Viccaro, 2017; Cannata et al., 2018; Ubide and Kamber, 2018; Viccaro et al., 2019; Borzì et al., 2020). Despite a diffusion only calculation will produce overestimated timescales, it is reasonable to adopt such approach when modeling Mt. Etna dynamics because it allows catching a glimpse of the differences in time among subsequent processes of magmatic intrusion, which may have occurred over a given inspected period of activity.

3.3 Petrography of erupted products

Lava rocks and tephra have porphyritic texture and contain plagioclase, clinopyroxene, olivine and opaque oxides in order of abundance. The groundmass has generally hyalopilitic texture and contains microlites of the same mineral phases with higher abundance of plagioclase with respect to olivine, clinopyroxene and opaque oxides. Plagioclases form the 30-45 vol.% of crystals, olivines are the 5-15 vol.%. Clinopyroxenes are augitic in composition and compose <35 vol.% of the total crystal content. Opaque oxides are titaniferous magnetites and compose <7 vol.% of the total crystal content, occurring mainly in the groundmass. The crystal content varies from about 30 vol% in samples erupted on July 27-28 and progressively decreases throughout the eruptive phases of November-December 2019, finally reaching ~20 vol.% in the latest samples of January 24.

3.4 Plagioclase textures and zoning

Plagioclase, the dominant mineral phase in all samples, covers all the dimensional classes, conventionally subdivided into small (<0.4 mm along the apparent c axis), medium (0.5–1.2 mm) and

large (>1.5 mm). The proportion of these size-groups, as well as related textures and zoning, varies in each sample. Any single plagioclase crystal can display more than one texture, along with a variety of zoning patterns from core to rim. Moreover, different textural types are found superimposed on each other. For simplicity, the most relevant chemical and textural characteristics of plagioclase have been synthetized as follows and illustrated in **Fig. 2**: a) Clear fine-scale (~1 mol% An) oscillatory zoning (OZp) extending across the entire core-to-rim profile (**Fig. 2a**) or just along discrete zones of plagioclase (**Fig. 2c-f**); b) An-rich rounded cores with coarse sieve textures (CS). The magnitude of resorption varies significantly among crystals in a way that the resorption sometimes extends across most of the crystal length (CS1), except at the outermost rim (**Fig. 2b,f**). Other crystals have incipient resorption (CS2), which affects just the inner core (**Fig. 2c**); c) Clear An-rich rounded cores bounded by dissolution surfaces (DC; **Fig. 2d**); d) Spongy sieve-textures of various widths from 30 to 150 μm (ST) developing at the outermost rim or in discrete zones intermediate between core and rim **(Fig. 2e,f)**.

Medium and large-size crystals often display pervasive resorption, especially at the core (CS1), and show major dissolution surfaces between discrete zones having distinct average An concentration. The An content across CS cores ranges between 70 and 85 mol%, then it falls abruptly to ~50 mol% in correspondence of the dissolution surface. Rims may be entirely oscillatory zoning (An_{44-58}) or, more commonly, they preserve extensive (up to 150 μm wide) resorption textures (ST) at high An composition (An_{71-82}). Some of the largest crystals also preserve clear oscillatory zoned cores embedded within a ST zone that sometimes occurs in multiple layers.

Small-size crystals are typically clear oscillatory zoned along the entire profile (OZp). Otherwise, they display dissolved (DC) and/or slightly resorbed cores with coarse sieve textures (CS2) at high An content (~80 mol%). Rims display limited An variations in the range 45-56 mol%, without any evidence of dissolution/resorption textures.

The inspection of major oxides across distinct textural types has put into evidence overall concomitant trends between iron and An for OZp, CS and DC plagioclase crystals of different sizes (**Fig. 2; Supplementary Material 1**). For these textural types, FeO oscillates in the range 0.5-1.0 wt.%, showing concentrations that vary in accordance with An values. Peaks at higher FeO content up to 1.2 wt.% are only observed in correspondence of large ST textures, where An also increases compared to the adjacent zones. Contrariwise, plagioclase rims affected by just incipient resorption (e.g., 30-50 μm-wide ST) preserve rather constant FeO composition that does not increase at increasing An values (**Supplementary Material 1**).

Fig. 3 shows how the textural characteristics of plagioclase are distributed throughout the studied period. Rounded coarse-sieved cores (CS) are dominant in all samples. The highest abundance of CS textures characterizes plagioclase erupted at NSEC on July 2019 (~70%), then CS cores decrease

slightly over time to a minimum of ~50% in the January 2020 tephra. Clear oscillatory zoned cores also show a different distribution over time. OZp cores comprise 20% of crystals in July, while they are 20% to 40% between November 2019 and January 2020. Moreover, we observed a higher percentage (~30%) of crystals with core-to-rim oscillatory zoning in lava rocks erupted at VOR compared to those of NSEC. The presence of DC cores, only affected by dissolution, is limited to the samples of July and November 2019. Both the NSEC and VOR plagioclase crystals have plenty of ST rims, which distribute with similar percentage of 50% in all samples. In spite of the evidence of changes in the general distribution of plagioclase textures in time, there is no evidence of changes in time of the major element composition (An and FeO wt.%) within any single texture.

3.5 Olivine zoning

Olivine compositions vary from Fo_{68} to Fo_{83} mol%. The array of Fo chemical profiles across olivines reveals a variety of zoning patterns that can be categorized as follows: a) core-to-rim rather homogeneous Fo profiles with Fo variation within 1 mol% (OZ; **Fig. 4a**); b) homogeneous core composition and normally zoned rims (N; **Fig. 4b-c**); c) homogeneous core composition and reversely zoned rim (R; **Fig. 4d**); d) flat core profiles changing to normal plus reverse zoning toward the crystal edge (N+R; **Fig. 4e**); e) flat core profile changing to reverse zoning, and finally shifting to normal toward the edge (R+N; **Fig. 4f**). Both the normal and reverse zoning patterns may follow either sharp (up to 10 mol% in less than 20 μm) or gradual changes in Fo concentrations. The abundance of such types of zoning profiles and the percentage of olivine crystals having a given Fo concentrations at the core significantly vary throughout the whole period under investigation (**see Fig. 5; Supplementary Material 2**). For instance, the core composition of olivine crystals erupted at NSEC on July 27-28 spans the range Fo_{75-81}, with a peak of 86% of compositions between Fo_{75} and Fo_{77}. Most of the observed chemical profiles (~56% of the total olivine from the eruption of July 27-28) dominantly displays complex zoning, given by a sequence of normal plus reverse zoning (N+R) or reverse (up to Fo_{80}) plus normal zoning patterns (R+N), otherwise they display simple normally zoned rims (N; ~38%). The patterns of normal zoning in olivine from July 2019 always occur with sharp Fo variations up to 10 mol% (e.g. from Fo_{78-79} mol% to Fo_{68-74} mol%) in less than 20 μm. Crystals characterized by rather homogeneous Fo compositions along the whole core-to-rim profiles (OZ) are only the 8% of total olivines, while simple reversely zoned crystals (R) completely lack (**Fig. 5**).

The beginning of the activity at VOR on September 2019 marks a change in the general distribution of olivine core compositions, which drop on average to lower Fo contents. As a whole, the range of compositions cluster into four dominant ranges: Fo_{68-72}, Fo_{74-76}, Fo_{78} and Fo_{80} (**Fig. 5**). The composition Fo_{68-72} is by far the most abundant, affecting more than 60% of olivine cores erupted at VOR in the months of November and December 2019 and, later, on January 2020. Other

compositions >Fo_{74} are poorly represented and occur in variable proportions, which are anyway always less than 20% for each period of activity.

A change in the relative frequency of the major zoning types is also evident (**Fig. 5**). OZ is the dominant zoning type in olivine crystals erupted at VOR. The OZ olivine is largely present in the eruptive products of November (~50% of the total olivine abundance) and December 2019 (~55%), slightly decreasing in abundance (to ~27%) only in January 2020. The OZ-type only occurs with Fo variations confined between 68 and 72 mol%. Complex zoning crystals (N+R and R+N types) represent less than 20% of all olivine crystals in different eruptions. There is also evidence of a progressive decrease in abundance of N-type crystals (simple normal zoning) in the period November 2019 - January 2020 (from 50% to 9%). Contrariwise the abundance of R-type crystals (simple reverse zoning) gradually increases from 10 to ~27% over the same period. Compared to chemical features observed for the eruption of July 27-28, the Fo changes related to normal or reverse zoning patterns in olivines erupted at VOR are not sharp; rather the Fo content shows gradual changes (i.e., decreasing from Fo_{82} to Fo_{68-72} mol% in N zoning or increasing from Fo_{67-70} to Fo_{80} mol% in R zoning) over a crystal length of up to ~150 μm. Sharper Fo variations over small crystal length (less than 20 μm) are also observed, thought they are confined to the outer rim of a few crystals (cf. **Supplementary Material 2**).

4. Geophysical results

4.1 Data and methods

At Mt. Etna, volcanic tremor can be considered as the geophysical signal best reflecting the evolution of the volcanic activity. It has been shown how changes in amplitude, spectral content and source location of volcanic tremor accompany variations in volcano activity (Cannata et al., 2013 and references therein). Hence, volcanic tremor has been widely used for investigating the volcano dynamics and the plumbing system structure (e.g., Cannata et al., 2010, 2018; Viccaro et al., 2014, 2016c), as well as implementing automatic monitoring systems (e.g., Cannavò et al., 2017; Spampinato et al., 2019). Information to achieve both these tasks are also provided by infrasound signals, which allow studying degassing/explosive activity and reconstructing the shallowest portions of the plumbing system and their evolution over time (e.g., Sciotto et al., 2011; Watson et al., 2020).

Volcanic tremor, recorded during March 2019 – January 2020 by the permanent seismic network run by Istituto Nazionale di Geofisica e Vulcanologia, Osservatorio Etneo (INGV-OE), was analyzed. We made use of the seismic signals recorded by 16 stations (**Fig. 1a**), equipped with broadband (40 s cutoff period), three-component Trillium seismometers (Nanometrics^{TM}), acquiring in real time at a sampling rate of 100 Hz. Infrasound data were recorded by a network of 9 infrasonic stations,

equipped with GRASS 40AN microphones, with a flat response in the frequency range 0.3–20,000 Hz, acquiring at a sampling rate of 50 Hz (**Fig. 1a**).

Time evolution of volcanic tremor in terms of source location and amplitude has been investigated as follows (**Fig. 6**). The location of the volcanic tremor source centroid was constrained with a temporal resolution of 30 minutes by applying a grid search method based on the seismic amplitude decay with distance (for details see Di Grazia et al., 2006 and Cannata et al., 2013). In particular, the frequency band 0.5-2.5 Hz, where most of volcanic tremor energy is concentrated at Mt. Etna (Cannata et al., 2013), was taken into account. As for the volcanic tremor amplitude, it was estimated directly from the location algorithm, that provided a root mean square (RMS) amplitude value, reduced at 1 km from the centroid location, per each 30-minute-long window.

As for infrasound, we focused on amplitude transients, that were automatically detected by STA/LTA (Short Time Average/Long Time Average) algorithm and located by a grid-search technique based on the brightness function (e.g., Cannata et al., 2013; Kao and Shan, 2004; **Fig. 7**). In particular, regarding the detection, the STA/LTA algorithm was applied separately on the infrasound continuous signal recorded by all the available stations in two different frequency bands 0.1 - 1.0 Hz and 1 - 6 Hz. In the former band, the STA and LTA lengths were set equal to 1.5 and 15 s respectively, while in the latter band 0.5 and 5.0 s. If at least 3 stations detected an event (i.e. the STA/LTA ratio was higher than the threshold fixed to 2.8) within the same 20-s-long time window, the event was counted and the source location was carried out.

4.2 Results

During the investigated interval, volcanic tremor source centroid was located below the summit area at shallow depth (generally >2 km a.s.l.; **Fig. 6**). The short-lived periods showing the highest amplitudes coincide with explosive episodes, among which May 30, July 18-20 and 27-28 2019, when explosive activity took place in the NSEC area, September 9-11, 2019 at NEC and September 12, 2019 at VOR. During each of the aforementioned episodes, the centroid of volcanic tremor sources migrated towards the eruptive vent. In addition, it has been also possible to observe longer-term variations: i) amplitude and centroid altitude increase, which took place in April 2019; ii) further amplitude increase in August-September 2019; iii) slight deepening in centroid altitude in December 2019.

Concerning infrasound data, about 27,500 events were detected and located. The infrasound event daily number, as well as their reduced amplitude, reached the highest values during the period encompassing September-October 2019 **(Fig. 7b)**. **Fig. 7** highlights that all the main summit crater areas (SEC/NSEC, VOR, BN and NEC) radiated infrasound. In particular, the first one generated infrasound mostly during the explosive activity of July 2019, VOR during September-October 2019,

while BN and NEC discontinuously during April-October 2019 and September 2019 – January 2020, respectively. The highest values of reduced amplitudes were recorded during the explosive activity at SEC/NSEC and VOR (**Fig. 7**).

5. Discussion

5.1 Architecture and dynamics of the pre-2019 Mt. Etna plumbing system

A weak explosive behavior characterized by Strombolian and effusive activity has been stated as the typical eruptive manifestation of Mt. Etna following the paroxysms of 2015-2016. This behavior is thought to be dominantly controlled by pressure imbalances affecting a large section of the plumbing system, which can result in persistent eruptive activity at the summit (such as during the activity of February-April 2017 at NSEC; Viccaro et al., 2019) or during flank eruptions (e.g., the eruption of December 24-27, 2018; Borzì et al., 2020). Petrological and geophysical data available for the volcanic activity that immediately preceded the beginning of eruptions at NSEC in 2019, indicated a two-year long period of continuous replenishment of the mid-upper part of the volcano plumbing system, finally culminating with fracture opening and lava effusions at the base of NSEC on December 24, 2018 (Bonforte et al., 2019; Cannavò et al., 2019; De Novellis et al., 2019; Borzì et al., 2020; Giampiccolo et al., 2020; Pezzo et al., 2020). Major pressurization of the volcano edifice was detected between 290-120 MPa (~7-5 km b.s.l.; Borzi et al., 2020), a range coinciding with the interval of crystallization of Fo_{75-78} olivines.

Thermodynamic constraints on the crystallization conditions of compositionally-distinct crystal populations have been provided for different eruptions of Mt. Etna recent activity, allowing discerning among some main, physically-separated, magmatic environments that appear to be variably connected to each other. In pioneer works, Kahl et al. (2011, 2013, 2015) support a mechanism of multi-level magma transfer between distinct magmatic environments to have fed the Etnean eruptions between 1991-2008. Later, Giuffrida and Viccaro (2017) applied a similar methodology to unravel magma dynamics over the 2011-2013 eruptive period, refining the set of intensive variables associated to the previously identified environments. These authors also extended the inspection of the plumbing system to the deeper parts of the edifice (≥20 km), in accordance with the observation of Mg-richer compositions in olivine, which they associate to more basic environments. Since then, thermodynamic constraints provided by Giuffrida and Viccaro (2017) have been routinely used to assess crystallization conditions of the whole range of olivine compositions recently erupted at Mt. Etna (e.g., Viccaro et al., 2016c; Cannata et al., 2018; Viccaro et al., 2019; Borzì et al., 2020).

The interpretation of data presented in this study for the 2019 - 2020 eruptions builds upon what we know about Etna's plumbing system architecture, as inferred from the updated post-2011 crystal

chemistry analyses and modelling. In reference to the 2018 period, magmas feeding the eruption were stored at the conditions of two magmatic environments, labeled M1a and M1b by Giuffrida and Viccaro (2017), which primarily acted as reservoirs accommodating continuous magma recharge from a lower environment M0. Physical characteristics of the detected environments are expressed by a set of key intensive variables. Specifically, M1b (T=1104-1112°C; P=120-160 MPa; fO_2=5.9-4.7x10^{-10} bars) denotes the environment of crystallization of an olivine population having Fo_{78} cores; M1a (T=1126-1136°C; P=230-290 MPa; fO_2=1.4-1.0x10^{-9} bars) refers to a Fo_{75-76} olivine core population; M0 (T=1156-1160°C; P=380-400 MPa; fO_2=3.5-3.0x10^{-9} bars) relates to the Fo_{80-82} compositions (**Fig. 8a**). It was also recognized a very shallow environment, named M2, encompassing thermodynamic conditions of the Fo_{70-73} olivine cores. Subsurface storage and crystallization at the conditions of M2 (T≤1088°C; P≤30 MPa; fO_2≤2.3x10^{-10} bars), while continuously documented throughout the eruptions of last decade (Cannata et al., 2018; Viccaro et al., 2016c, 2019), did not arise from the inspection of olivines from the Christmas 2018 eruption, as magmas migrated laterally bypassing the very shallow central system. At the same time, there was no evidence for activation of deepest magmatic environments (i.e., M00 and Mx) recognized during the 2015-2018 eruptive period (Cannata et al., 2018; Viccaro et al., 2019; Borzì et al., 2020).

5.2. The sequence of 2019-2020 events from a crystal-chemistry plus geophysical perspective

Chemical characteristics of olivine erupted at NSEC during July 2019, with almost all core compositions clustered in the range Fo_{75-77}, give us evidence that conditions of magma storage in the mid-upper plumbing system did not change too much with respect to 2018. This also suggest that the same section of the plumbing system between 290-120 MPa was involved as the principal site of magma accumulation. This finding agrees with the evidence from geophysical studies (Bonaccorso et al., 2011; Patanè et al., 2013) of a main, vertically-extended zone of magma storage and differentiation at ~2-6 km b.s.l., constituting the intermediate section of Etna plumbing system. Aside from cores, a large heterogeneity is evident in terms of compositional variations toward the rims of olivine erupted on July 27-28, 2019, being complex zoning (R+N and N+R) the most characteristic zoning types within the core group at Fo_{75-77}. The sequence of reverse and normal zoning in these crystals testifies that the hosting magmatic environments (i.e. M1a and M1b) were very active before the NSEC eruption, suffering replenishment phases with magmas uprising from a deeper, more basic environment (M0), as well as episodes of intrusion at low pressure (<40 MPa). The latter are indicated by normally zoned rims typically re-equilibrating at Fo_{70-74}, in accordance with the composition of M2. The large instability of the resident system at higher pressure (i.e., 290-120 MPa) due to mechanisms of magma recharge is consistent with the observation of plagioclase cores recording major episodes of destabilization that primarily manifest as CS textures, along which a good positive

correlation between An and FeO% is evident (Eichelberger, 1978; Tsuchiyama 1985; Tepley et al., 1999; Viccaro et al., 2010, 2016a).

We used elemental diffusion on zoned olivine erupted at NSEC to calculate the time at which the recharging phases involving the M1a and M1b environments began and led to the July 27-28, 2019 eruption (**Fig. 8b and 9; Supplementary Material 3**). Diffusion is one of the processes occurring during the pre-eruptive history of a crystal that can considerably modify its initial chemical zoning (Costa and Chakraborty 2004; Chakraborty, 2008; Costa et al., 2008; Zhang and Cherniak, 2010). Here, olivine zoning patterns were modeled under the assumption that diffusion had major control on the final profile. Therefore, we refer to the calculated timescales as to the times of diffusive re-equilibration of a given concentration profile toward new equilibrium conditions, as a consequence of a major event of destabilization (e.g., abrupt change in temperature and composition) of the host magmatic environment. For instance, the incorporation of an olivine in a recharging magma of more basic composition is thought to be responsible for increasing Fo concentration, and the diffusion time we obtain is that from the recharge event until the crystal is erupted. Instead, the olivine transfer and storage in a more differentiated environment will result in decreasing Fo and, in this case, the diffusion timescale will reflect the time that the crystal spent in the final environment before being erupted.

Following such assumptions, the diffusive relaxation of reverse zoning in olivine crystals from the July 27-28, 2019 eruption reproduces timescales of 28-41 ±8-12 days (**Table 1 and Supplementary Material 3**). This therefore indicates that the episodes of recharge in M1a and M1b happened during the second half of June 2019, between June 17-29. Over this period, there is no significant variation of the seismo-volcanic signals, as magma movements detected from crystals dominantly occurred at deep levels of the plumbing system.

The analysis of variations of the olivine zoning related to the activity at VOR emphasizes the beginning of a persistent Strombolian activity driven by recharge/discharge phases that affect mostly the shallowest, most differentiated section of the Mt. Etna plumbing system. Given the large number of Fo_{68-72} olivine core compositions erupted from November 2019 to January 2020, we can assert that the zone of major crystallization and accumulation of magma covers a range of pressure from ~40 MPa (~2 km of depth below the summit) to the surface. Noteworthy, the composition of such large group of olivines spans over a more evolved chemical range than that constrained thermodynamically for M2 (cf. Giuffrida and Viccaro, 2017). At shallow levels, magmas were stored without experiencing important chemical and physical perturbations (e.g., due to magma recharge) as those recorded before the eruption of July 27-28 at NSEC. Indeed, tephra erupted at VOR are rich of crystals having textural and chemical features reflecting crystallization under dominant equilibrium conditions. We found an increasing number of low-An oscillatory zoning plagioclase cores (OZp)

coexisting with low-Fo, compositionally-homogeneous olivines (OZ) especially in tephra of November and December 2019 (**Figs. 2-4**), which emphasize the overall stability of volcanic phenomena at VOR during the whole period of activity (Allègre et al., 1981; Ginibre et al., 2007; Giuffrida et al., 2020; Kohn et al., 1989; Viccaro et al., 2010, 2016a). The typical situation producing a profile at rather constant composition in a single crystal is when the crystal experiences crystallization in a unique magmatic environment under rather stable physical and chemical conditions (Allègre et al., 1981; Ginibre et al., 2002, 2007; Kohn et al., 1989; Bouvet de Maisonneuve et al., 2016). Thus, the occurrence of abundant entirely unzoned olivines, all having Fo between 68-73 mol%, proofs that these crystals resided at low pressure potentially for a long time before being erupted. This feature also suggests that magmas feeding the Strombolian manifestations at VOR moved fast directly toward surface without stalling into the conduit, so that the olivine rims had no time to completely re-equilibrate at more differentiated magmatic compositions (Coombs and Gardner, 2004; Costa et al., 2013; Bouvet de Maisonneuve et al., 2016).

Observed variations in plagioclase and olivine features change in accordance with the evolution of volcanic activity at VOR. Indeed, the higher frequency of the volcanic activity observed since January 2020 results in increasing number of plagioclases affected by disequilibrium textures either at cores or rims (i.e., CS, ST and CS+ST textural types; **Figs. 2 and 3**), while olivine with distinct core composition mostly shows reverse zoning (R or R+N types; **Figs. 4 and 5**). Note that plagioclase sieve textures have peaks in both An and FeO wt.%, as an indication that changing magmatic compositions, possibly due to recharge into the resident system, was likely the cause of crystal resorption (Tsuchiyama, 1985; Ginibre and Worner, 2007; Viccaro et al., 2010, 2016a). In olivine crystals, reverse zoning patterns indicate two distinct phases of mafic recharge, one involving Fo_{77-78} cores with increasing gradient up to Fo_{82}, and a second affecting the more evolved Fo_{68-72} cores. We interpret the progressive changes of mineral compositions and zoning with the eruption sequence to reflect the transition from an early phase (between November and December 2019) characterized by more stable conditions of magma transport toward an activity (from the beginning of January 2020) driven by episodes of deep replenishment by more mafic M0 magmas that push upward the resident one (stored at the conditions of M1a and M1b). This interpretation is consistent with the calculated diffusion timescales for olivine crystals erupted throughout the period of activity of VOR (**Fig. 9; Table 1; Supplementary Material 3**). We calculated timescales of weeks to few days for olivine erupted on January 24, 2020. The longest timescales (23-30 ±3-9 days) derive from modeling the reverse zoning patterns in olivine at high-Fo cores, meaning that early episodes of deep replenishments must have approximately occurred between December 26, 2019 and January 1, 2020. Instead, the intrusion at shallow levels started shortly before the eruption on January 24, as we recovered diffusion times of just 2-11 ±1-3 days from modeling the reverse zoning in olivine at low-

Fo core composition. Compared to what crystals of January 2020 reveal, we find that most of the zoned olivines from the November-December 2019 eruptions record mechanisms of chemical re-equilibration at variable physical and chemical conditions that lasted for several months before the crystals were erupted. Specifically, the calculated timescales refer to shallow magmatic intrusions dating back to the beginning of May and to the second half of June (around June 20-25). The latter period is in agreement with timescales of magmatic recharge recorded by olivine crystals erupted on July 27-28 at NSEC. Diffusion timescales for the period November-December 2019 also evidence short-term processes of magma transport and olivine re-equilibration at low pressure that refer to October 23-29 and December 1, therefore evidencing recharge episodes that are directly related to eruptions of November 4 and December 19, respectively (**Table 1; Supplementary Material 3**).

There also exists a correlation between petrological data, seismo-volcanic signals, and temporal evolution of volcanic activity, as evidenced by volcanic tremor and infrasonic event patterns (**Fig. 8b**). Volcanic tremor allows the inspection of the shallow portions of the plumbing system (above ~2 km a.s.l.), whereas infrasonic events provide information on the uppermost parts of this shallow plumbing system coinciding with the main craters that gave rise to both eruptive and degassing activities. The first important variation of volcanic tremor took place in April 2019 and mainly consisted of an increase in amplitude (**Figs. 6** and **8b**). This change, which followed the gradual tremor amplitude decrease occurring after the December 24-27, 2018, flank eruption (see INGV-OE Internal Report, 2019d), could be due to the increasing supply of gas in the plumbing system. Indeed, as suggested by Girona et al. (2019), who explored the source mechanism of shallow tremor by examining the dynamics of gas pockets trapped beneath permeable media, the amplitude of volcanic tremor is affected by the amounts of volatiles reaching the shallow part of the plumbing system. Successively, in mid-September 2019 source locations of volcanic tremor and infrasound events confirm that explosive activity shifted from the SEC/NSEC complex toward the NEC and VOR (**Figs. 6** and **7**). Volcanic activity at VOR was preceded by a gradual volcanic tremor amplitude increase starting from mid-August and from resumption of activity at NEC (**Fig. 8b**). As VOR began erupting on September 12, 2019, the tremor amplitude rapidly increased, while its centroid altitude remained constant at very shallow depth (> 2.5 km a.s.l.; **Fig. 6**). Again, the observed increase in volcanic tremor amplitude from mid-August could be caused by a further increase of volatiles reaching the shallow part of the plumbing system. Such a phenomenon of uprise of gas/gas-rich magma could also justify the concomitant reactivation of VOR.

Further clues of changes in the plumbing system conditions, likely deriving from enrichment in volatiles and pressurization, come from infrasound. The NEC started emitting again infrasonic events on September 9 and from then on (**Fig. 7b,d**). NEC has been considered as the main source of infrasound at Mt. Etna since the installation of the first permanent microphone at Mt. Etna in 2006.

It has been shown how changes in the spectral content of the NEC infrasound events often precede or follow eruptive activity at other craters, especially at SEC/NSEC (e.g., Sciotto et al., 2011; Spina et al., 2015). In particular, the source modelling of infrasound events has allowed inferring variations in the NEC plumbing system in terms of shallowing or deepening of magma level caused by the eruptive activity at SEC/NSEC and then by the interconnection between SEC/NSEC and NEC feeding systems (e.g., Sciotto et al., 2011; Spina et al., 2015). The reappearance of NEC infrasonic events concomitant with the reactivation of VOR also suggests how their feeding systems are connected. It confirms the importance of the monitoring of the NEC infrasonic activity in detecting the changes taking place in the shallow plumbing system not only feeding SEC/NSEC but all the summit craters.

A deepening of the volcanic tremor source centroid was observed starting from mid-December 2019, in accordance with the evidence of mafic replenishments from deeper environments resulting from the analysis of olivine zoning and diffusion profiles **(Fig. 8b).** Indeed, this deeper source of volcanic tremor could be caused by the uprise of more mafic magma batch, whose gas component plays an important role in generating shallow volcanic tremor (Girona et al., 2019). Hence, volcanic tremor and infrasound data provide information about the distinct pathways of magma migration feeding the summit craters, as well as their interconnections at depth.

6. Concluding remarks

A spatial and temporal reconstruction of magma dynamics driving the activity at Mt. Etna between mid-2019 and January 2020 has been achieved by adopting a multidisciplinary approach, which combines petrological data, volcanic tremor, and infrasound data. Multiple episodes of magma recharge from deep portions of the plumbing system with consequent intrusion into intermediate-to-shallow levels were detected starting from May 2019. Magmatic recharge was detected in consequence of an episode of intensification of volcanic tremor that led the tremor amplitude to higher level for most of the remaining investigated period. Such signals were precursory of the eruptive episodes of May and July 2019 at NSEC. The following reactivation of VOR since mid-September 2019 chiefly involved magmas coming from a nearly unperturbed magmatic environment located at pressure lower than 40 MPa, which fed a steady-state Strombolian and effusive activity at the summit for several months. Such persistent activity changed to more continuous Strombolian explosions in January 2020 in response of episodic migration of deeper magmas to the shallow reservoir.

The changes in the state of volcanic activity observed during the 2019-2020 period agree with the evidence of continuous magma replenishment affecting the plumbing system since the end of paroxysmal activity at VOR in May 2016. As already observed at Mt. Etna during previous eruptions, intrusive episodes at shallow levels following prolonged periods of deep replenishment are usually precursory to the reactivation of the summit craters (i.e., Di Grazia et al., 2009; Patanè et al., 2013;

Bonforte et al., 2017; Ubide and Kamer, 2018). In this regard, the beginning of volcanic activity in 2019 was preceded by a two-years long period of relative quiescence at Mt. Etna, during which the central feeding system was constantly refilled by injection of new mafic magmas. Despite the evidence of conspicuous magma recharge, only limited volumes of magmas were emitted during the 2018 flank eruption (Bonforte et al., 2019; Alparone et al., 2020; Borzì et al., 2020). These events created proper conditions to the onset of the new eruptive phase characterizing the Mt. Etna summit craters in 2019. Indeed, renewal of the activity at NSEC since May 2019 may be viewed as the response of a pressure imbalance between the intermediate and the shallowest part of the volcano feeding system that promote the drainage of magmas toward shallow reservoirs, followed by the eruption. The NSEC reactivation allowed re-establishing a mechanism of steady-state recharge/discharge of plumbing system, powered by continuous magmatic intrusion. This mechanism seems to be recurrent in the post-2016 volcanic record (Currenti and Bonaccorso, 2019; Viccaro et al., 2019). Repeated intrusions from depth pushed out the magma stored in the shallow storage zones, leading to the persistent activity observed at VOR throughout the last months of 2019. Thus, the steady-state activity reflects dynamics of magma recharge from depths that are counterbalanced, at present, by discharge of magma residing in the shallowest reservoirs. Since April 2020, the persistent Strombolian activity shifted at NSEC, suggesting that magma replenishment continued through 2020. Results of this study confirm a continuously evolving plumbing system scenario, characterized by short-term changes in magma supply rates and storage conditions that have direct, often immediate consequences on the state of volcanic activity.

Acknowledgements

This work was supported by the funding program PIACERI 2020-22 of the University of Catania (PAROSSISMA project, code 22722132140; principal investigator M. Viccaro). The Authors greatly acknowledge the Editor in Chief Diana Roman for the handling of the manuscript and two anonymous reviewers for their useful suggestions.

References

Aiuppa, A., Moretti, R., Federico, C., Giudice, G., Gurrieri, S., Liuzzo, M., Papale, P., Shinohara, H., Valenza, M., 2007. Forecasting Etna eruptions by real-time observation of volcanic gas composition. Geology 35, 1115-1118. https://doi.org/10.1130/G24149A.1

Aiuppa, A., Burton, M., Caltabiano, T., Giudice, G., Guerrieri, S., Liuzzo, M., Murè, F., Salerno, G., 2010. Unusually large magmatic CO_2 gas emissions prior to a basaltic paroxysm. Geophys. Res. Lett. 37, 5. https://doi.org/201010.1029/2010GL043837

Aiuppa, A., Cannata, A., Cannavò, F., Grazia, G.D., Ferrari, F., Giudice, G., Gurrieri, S., Liuzzo, M., Mattia, M., Montalto, P., Patanè, D., Puglisi, G., 2010. Patterns in the recent 2007-2008 activity of Mount Etna volcano investigated by integrated geophysical and geochemical observations. Geochem. Geophys. Geosyst. 11, 13. https://doi.org/201010.1029/2010GC003168

Allègre, C.J., Provost, A., Jaupart, C., 1981. Oscillatory zoning: a pathological case of crystal growth. Nature 294, 223-228. https://doi.org/10.1038/294223a0

Alparone, S., Barberi, G., Giampiccolo, E., Maiolino, V., Mostaccio, A., Musumeci, C., Scaltrito, A., Scarfì, L., Tuvè, T., Ursino, A., 2020.Seismological constraints on the 2018 Mt. Etna (Italy) flank eruption and implications for the flank dynamics of the volcano. Terra Nova 32, 334-344. https://doi.org/10.1111/ter.12463

Behncke, B., Branca, S., Corsaro, R. A., De Beni, E., Miraglia, L., Proietti, C., 2014. The 2011–2012 summit activity of Mount Etna: Birth, growth and products of the new SE crater, J. Volcanol. Geotherm. Res., 270, 10–21.

Bonaccorso, A., Bonforte, A., Calvari, S., Del Negro, C., Di Grazia,G., Ganci, G., Neri, M., Vicari, A., Boschi, E., 2011. The initial phases of the 2008–2009 Mount Etna eruption: A multidisciplinary approach for hazard assessment, J. Geophys. Res. 116, B03203.

Bonforte, A., Fanizza, G., Greco, F., Matera, A., Sulpizio, R., 2017. Long-term dynamics across a volcanic rift: 21 years of microgravity and GPS observations on the southern flank of Mt. Etna volcano. J. Volcanol. Geotherm. Res. 344, 174-184.

Bonforte, A., Guglielmino, F., Puglisi, G., 2019. Large dyke intrusion and small eruption: The December 24, 2018 Mt. Etna eruption imaged by Sentinel-1 data. Terra Nova 31, 405–412. https://doi.org/10.1111/ter.12403

Borzì, A.M., Giuffrida, M., Zuccarello, F., Palano, M., Viccaro, M., 2020. The Christmas 2018 Eruption at Mount Etna: Enlightening How the Volcano Factory Works Through a Multiparametric Inspection. Geochem. Geophys. Geosyst. 21, e2020GC009226. https://doi.org/10.1029/2020GC009226

Bouvet de Maisonneuve, C., Costa, F., Huber, C., Vonlanthen, P., Bachmann, O., Dungan, M.A., 2016. How do olivines record magmatic events? Insights from major and trace element zoning. Contrib. Mineral. Petrol. 171, 56. https://doi.org/10.1007/s00410-016-1264-6

Branca, S., Del Carlo, P., 2005. Types of eruptions of Etna volcano AD 1670-2003: implications for short-term eruptive behaviour. Bull. Volcanol. 67, 732-742. https://doi.org/10.1007/s00445-005-0412-z

Calvari, S., Cannavò, F., Bonaccorso, A., Spampinato, L., Pellegrino, A.G., 2018. Paroxysmal explosions, lava fountains and ash plumes at Etna volcano: eruptive processes and hazard implications. Front. Earth Sci. 6, 107. https://doi.org/10.3389/feart.2018.00107

Cannata, A., Di Grazia, G., Montalto, P., Ferrari, F., Nunnari, G., Patanè, D., Privitera, E., 2010. New insights into banded tremor from the 2008–2009 Mount Etna eruption. J. Geophys. Res. Solid Earth 115, B12318. https://doi.org/10.1029/2009JB007120

Cannata, A., Di Grazia, G., Aliotta, M., Cassisi, C., Montalto, P., Patanè, D., 2013. Monitoring seismo-volcanic and infrasonic signals at volcanoes: Mt. Etna case study. Pure Appl. Geophys. 170, 1751–1771. https://doi.org/10.1007/s00024-012-0634-x

Cannata, A., Di Grazia, G., Giuffrida, M., Gresta, S., Palano, M., Sciotto, M., et al. 2018. Space-time evolution of magma storage and transfer at Mt. Etna volcano (Italy): The 2015–2016 reawakening of Voragine crater. Geochem. Geophys. Geosyst. 19, 471–495. https://doi.org/10.1002/2017GC007296

Cannavò, F., Cannata, A., Cassisi, C., Di Grazia, G., Montalto, P., Prestifilippo, M., Privitera, E., Coltelli, M., Gambino, S., 2017. A multivariate probabilistic graphical model for real-time volcano monitoring on Mount Etna. J. Geophys. Res. Solid Earth. 122, 3480-3496. https://doi.org/10.1002/2016JB013512

Cannavò, F., Sciotto, M., Cannata, A., Di Grazia, G., 2019. An integrated geophysical approach to track magma intrusion: the 2018 Christmas eve eruption at Mt. Etna. Geophys. Res. Letters 46, 8009–8017. https://doi.org/10.1029/2019GL083120

Cashman, K.V., 1990. Textural constraints on the kinetics of crystallization of igneous rocks. Rev. Mineral. Geochem. 24, 259-314.

Chakraborty, S., 2008. Diffusion in solid silicates: A tool to track timescales of processes comes of age. Ann. Rev. Earth Plan. Sci. 36, 153-190. https://doi.org/10.1146/annurev.earth.36.031207.124125

Coombs, M.L., Gardner, J.E., 2004. Reaction rim growth on olivine in silicic melts: Implications for magma mixing. Amer. Mineral. 89, 748–758. https://doi.org/10.2138/am-2004-5-608

Corsaro, R.A., Miraglia, L., 2005. Dynamics of 2004-2005 Mt. Etna effusive eruption as inferred from petrologic monitoring. Geophys. Res. Lett. 32, 13. https://doi.org/10.1029/2005GL022347

Corsaro, R.A., Andronico, D., Behncke, B., Branca, S., Caltabiano, T., Ciancitto, F., Cristaldi, A., De Beni, E., La Spina, A., Lodato, L., Miraglia, L., Neri, M., Salerno, G., Scollo, S., Spata, G., 2017. Monitoring the December 2015 summit eruptions of Mt. Etna (Italy): Implications on eruptive dynamics. J. Volcanol. Geotherm. Res. 341, 53-69. https://doi.org/10.1016/j.jvolgeores.2017.04.018

Costa, F., Chakraborty, S., 2004. Decadal time gaps between mafic intrusion and silicic eruption obtained from chemical zoning patterns in olivine. Earth Planet. Sci. Lett. 227, 517-530.

Costa, F., Dohmen, R., Chakraborty, S., 2008. Timescales of magmatic processes from modeling the zoning patterns of crystals. Rev. Mineral. Geochem. 69, 545-594. https://doi.org/10.2138/rmg.2008.69.14

Costa, F., Andreastuti, S., Bouvet de Maisonneuve, C., Pallister, J.S., 2013. Petrological insights into the storage conditions, and magmatic processes that yielded the centennial 2010 Merapi explosive eruption. J. Volcanol. Geotherm. Res. 261, 209–235. https://doi.org/10.1016/j.jvolgeores.2012.12.025

Currenti, G., Bonaccorso, A., 2019. Cyclic magma recharge pulses detected by high-precision strainmeter data: the case of 2017 inter-eruptive activity at Etna volcano. Sci. Rep. 9, 7553. https://doi.org/10.1038/s41598-019-44066-w

Davidson, J.P., Tepley, F.J., 1997. Recharge in volcanic systems – Evidence from isotope profiles of phenocrysts. Science 275, 826-829. https://doi.org/10.1126/science.275.5301.826

Del Carlo, P., Pompilio, M., 2004. The relationship between volatile content and the eruptive style of basaltic magma: the Etna case. Ann. Geophys. 47, 4. https://doi.org/10.4401/ag-4402

De Novellis, V., Atzori, S., De Luca, C., Manzo, M., Valerio, E., Bonano, M., Cardaci, C., Castaldo, R., Di Bucci, D., Manunta, M., Onorato, G., Pepe, S., Solaro, G., Tizzani, P., Zinno, I., Neri, M., Lanari, R., Casu, F., 2019. DInSAR analysis and analytical modeling of Mount Etna displacements: The December 2018 volcano-tectonic crisis. Geophys. Res. Lett. 46, 5817–5827. https://doi.org/10.1029/2019GL082467

Di Grazia, G., Falsaperla, S., Langer, H., 2006. Volcanic tremor location during the 2004 Mount Etna lava effusion. Geophys. Res. Lett. 33, L04304. https://doi.org/10.1029/2005GL025177

Di Grazia, G., Cannata, A., Montalto, P., Patanè, D., Privitera, E., Zuccarello, L., Boschi E., 2009. A new approach to volcano monitoring based on 4D analyzes of seismo-volcanic and acoustic signals: The 2008 Mt. Etna eruption. Geophys. Res. Lett. 36, L18307. https://doi.org/10.1029/2009GL039567

Di Stefano, F., Mollo, S., Ubide, T., Petrone, C.M., Caulfield, J., Scarlato, P., Nazzari, M., Andronico, D., Del Bello, E., 2020. Mush cannibalism and disruption recorded by clinopyroxene phenocrysts at Stromboli volcano: New insights from recent 2003-2017 activity. Lithos 360-361, 105440. https://doi.org/10.1016/j.lithos.2020.105440

Dohmen, R., Chakraborty, S., 2007. Fe-Mg diffusion in olivine II: Point defect chemistry, change of diffusion mechanisms and a model for calculation of diffusion coefficients in natural olivine. Phys. Chem. Min. 34, 409–430. https://doi.org/10.1007/s00269-007-0158-6

Duncan, A.M., Chester, D.K., Guest, J.E., 1981. Mount Etna volcano: environmental impact and problems of volcanic prediction. Geograph. J. 147, 164-178. https://doi.org/10.2307/634532

Druitt, T.H., Costa, F., Deloule, E., Dungan, M., Scaillet, B., 2012. Decadal to monthly timescales of magma transfer and reservoir growth at a caldera volcano. Nature 482, 77-80. https://doi.org/10.1038/nature10706

Eichelberger, J.C., 1978. Andesitic volcanism and crustal evolution. Nature 275, 21-27. https://doi.org/10.1038/275021a0

Francalanci, L., Avanzinelli, R., Nardini, I., Tiepolo, M., Davidson, J.P., Vannucci, R., 2012. Crystal recycling in the steady-state system of the active Stromboli volcano: a 2.5-ka story inferred from in situ Sr-isotope and trace element data. Contr. Mineral. Petrol. 163, 109-131. https://doi.org/10.1007/s00410-011-0661-0

Giampiccolo, E., Cocina, O., De Gori, P., Chiarabba, C., 2020. Dyke intrusion and stress-induced collapse of volcano flanks: The example of the 2018 event at Mt. Etna (Sicily, Italy). Sci. Rep. 10, 6373. https://doi.org/10.1038/s41598-020-63371-3

Ginibre, C., Kronz, A., Wörner, G., 2002. High-resolution quantitative imaging of plagioclase composition using accumulated backscattered electron images: new constraints on oscillatory zoning. Contrib. Mineral. Petrol. 142, 436–448. https://doi.org/10.1007/s004100100298

Ginibre, C., Wörner, G., Kronz, A., 2007. Crystal zoning as an archive for magma evolution. Elements 3, 261-266. https://doi.org/10.2113/gselements.3.4.261

Ginibre, C., Wörner, G., 2007. Variable parent magmas and recharge regimes of the Parinacota magma system (N. Chile) revealed by Fe, Mg and Sr zoning in plagioclase. Lithos 98, 118-140. https://doi.org/10.1016/j.lithos.2007.03.004

Girona, T., Caudron, C., Huber, C., 2019. Origin of shallow volcanic tremor: the dynamics of gas pockets trapped beneath thin permeable media. J. Geophys. Res. Solid Earth 124, 4831-4861. https://doi.org/10.1029/2019JB017482

Giuffrida, M., Viccaro, M., 2017. Three years (2011–2013) of eruptive activity at Mt. Etna: Working modes and timescales of the modern volcano plumbing system from micro-analytical studies of crystals. Earth Sci. Rev. 171, 289–322. https://doi.org/10.1016/j.earscirev.2017.06.003

Giuffrida, M., Viccaro, M., Ottolini, L., 2018. Ultrafast syn-eruptive degassing and ascent trigger high-energy basic eruptions. Sci. Rep. 8, article number 147. https://doi.org/10.1038/s41598-017-18580-8

Giuffrida, M., Nicotra, E., Viccaro, M., 2020. Changing modes and rates of mafic magma supply at Pantelleria (Sicily Channel, Southern Italy): new perspectives on the volcano factory drawn upon olivine records. J. Petrol. 61, 5. https://doi.org/10.1093/petrology/egaa051

Gordeychik, B., Churikova, T., Kronz, A., Sundermeyer, C., Simakin, A., Wörner, G., 2018. Growth of, and diffusion in, olivine in ultra-fast ascending basalt magmas from Shiveluch volcano. Sci. Rep. 8, 11775. https://doi.org/10.1038/s41598-018-30133-1

Harris, A., Steffke, A., Calvari, S., Spampinato, L., 2011. Thirty years of satellite-derived lava discharge rates at Etna: Implications for steady volumetric output. J. Geophys. Res. Solid Earth 116, B8. https://doi.org/10.1029/2011JB008237

INGV-OE Internal Report (2019a). Etna Bollettino Settimanale 22/07/2019–28/07/2019, Rep. n° 31/2019, available at www.ct.ingv.it

INGV-OE Internal Report (2019b). Etna Bollettino Settimanale 28/10/2019–03/11/2019, Rep. n° 44/2019, available at www.ct.ingv.it

INGV-OE Internal Report (2019c). Etna Bollettino Settimanale 04/11/2019–10/11/2019, Rep. n° 45/2019, available at www.ct.ingv.it

INGV-OE Internal Report (2019d). Etna Bollettino Settimanale 07/01/2019-13/01/2019, Rep. n° 3/2019, available at www.ct.ingv.it

INGV-OE Internal Report (2019e). Etna Bollettino Settimanale 27/05/2019-02/06/2019, Rep. n° 23/2019, available at www.ct.ingv.it

INGV-OE Internal Report (2020a). Etna Bollettino Settimanale 06/01/2020–12/01/2020, Rep. n° 03/2020, available at www.ct.ingv.it

INGV-OE Internal Report (2020b). Etna Bollettino Settimanale 10/02/2020–16/02/2020, Rep. n° 08/2020, available at www.ct.ingv.it

INGV-OE Internal Report (2020c). Etna Bollettino Settimanale 27/04/2020–03/05/2020, Rep. n° 19/2020, available at www.ct.ingv.it

Kahl, M., Chakraborty, S., Costa, F., Pompilio, M., 2011. Dynamic plumbing system beneath volcanoes revealed by kinetic modeling, and the connection to monitoring data: An example from Mt. Etna. Earth Plan. Sci. Lett. 308, 11-22. https://doi.org/10.1016/j.epsl.2011.05.008

Kahl, M., Chakraborty, S., Pompilio, M., Costa, F., 2015. Constraints on the nature and evolution of the magma plumbing system of Mt. Etna volcano (1991–2008) from a combined thermodynamic and kinetic modelling of the compositional record of minerals. J. Petrol. 56, 2025–2068. https://doi.org/10.1093/petrology/egv063

Kahl, M., Chakraborty, S., Costa, F., Pompilio, M., Liuzzo, M., Viccaro, M., 2013. Compositionally zoned crystals and real-time degassing data reveal changes in magma transfer dynamics during the 2006 summit eruptive episodes of Mt. Etna. Bull. Volcanol. 75, art. 692. https://doi.org/10.1007/s00445-013-0692-7

Kahl, M., Viccaro, M., Ubide, T., Morgan, D., Dingwell, D.B., 2017. A branched magma feeder system during the 1669 eruption of Mt. Etna: evidence from a time-integrated study of zoned olivine phenocryst populations. J. Petrol. 58, 443-472. https://doi.org/10.1093/petrology/egx022

Kao, H., Shan, S.J., 2004. The source-scanning algorithm: Mapping the distribution of seismic sources in time and space. Geophys. J. Int. 57, 589–594. https://doi.org/10.1111/j.1365-246X.2004.02276.x

Kohn, S.C., Henderson, C.M.B., Mason, R.A., 1989. Element zoning trends in olivine phenocrysts from a supposed primary high-magnesian andesite: an electron- and ion-microprobe study. Contrib. Mineral. Petrol. 103, 242–252. https://doi.org/10.1007/BF00378510

Loomis, T.P., 1983. Compositional zoning of crystals: A record of growth and reaction history. In: Saxena S.K. (eds) Kinetics and equilibrium in mineral reactions. Adv. Phys. Geochem., vol 3. Springer, New York, NY. https://doi.org/10.1007/978-1-4612-5587-1_1

Luhr, J.F., Carmichael, I.S.E., 1990. Petrological monitoring of cyclical eruptive activity at Volcàn Colima, Mexico. J. Volcanol. Geotherm. Res. 42, 235-260. https://doi.org/10.1016/0377-0273(90)90002-W

Lynn, K.J., Garcia, M.O., Shea, T., Costa, F., Swanson, D.A., 2017. Timescales of mixing and storage for Keanakāko‘i Tephra magmas (1500–1820 C.E.), Kīlauea Volcano, Hawai‘i. Contrib. Mineral. Petrol. 172, 76. https://doi.org/10.1007/s00410-017-1395-4

Mangler, M.F., Prytulak, J., Gisbert, G., Delgado-Granados, H., Petrone, C.M., 2019. Interplinian effusive activity at Popocatépetl volcano, Mexico: New insights into evolution and dynamics of the plumbing system. Volcanica 2, 45–72. http://doi.org/10.30909/vol.02.01.4572

Mangler, M.F., Petrone, C.M., Hill, S., Delgado-Granados, H., Prytulak, J., 2020. A pyroxenic view on magma hybridization and crystallization at Popocatépetl Volcano, Mexico. Front. Earth Sci. 8, 362. https://doi.org/10.3389/feart.2020.00362

Martí, J., Castro, A., Rodríguez, C., Costa, F., Carrasquilla, S., Pedreira, R., Bolos, X., 2013. Correlation of magma evolution and geophysical monitoring during the 2011–2012 El Hierro (Canary Islands) submarine eruption. J. Petrol. 54, 1349–1373. https://doi.org/10.1093/petrology/egt014

Mutch, E.J.F., Maclennan, J., Shorttle, O., Edmonds, M., Rudge, J.F., 2019. Rapid transcrustal magma movement under Iceland. Nature Geosci. 12, 569-574.

Oeser, M., Ruprecht, P., Weyer, S., 2018. Combined Fe-Mg chemical and isotopic zoning in olivine constraining magma mixing-to-eruption timescales for the continental arc volcano Irazú (Costa Rica) and Cr diffusion in olivine. Am. Mineral. 103, 582-599. https://doi.org/10.2138/am-2018-6258

Palano, M., Viccaro, M., Zuccarello, F., Gresta, S., 2017. Magma transport and storage at Mt. Etna (Italy): A review of geodetic and petrological data for the 2002-03, 2004 and 2006 eruptions. J. Volcanol. Geotherm. Res. 347, 149-164. https://doi.org/10.1016/j.jvolgeores.2017.09.009

Pankhurst, M.J., Dobson, J., Morgan D.J., Loughlin, S.C., Thordarson, T., Lee P.D., Courtois, L., 2014. Monitoring the magmas fuelling volcanic eruptions in near-real-time using x-ray micro-computed tomography. J. Petrol. 55, 671-684. https://doi.org/10.1093/petrology/egt079

Pankhurst, M.J., Morgan, D.J., Thordarson, T., Loughlin, C., 2018. Magmatic crystal records in time, space, and process, causatively linked with volcanic unrest. Earth Plan. Sci. Lett. 493, 231-241. https://doi.org/10.1016/j.epsl.2018.04.025

Patanè, D., Aiuppa, A., Aloisi, M., Behncke, B., Cannata, A., Coltelli, M., Di Grazia, G., Gambino, S., Gurrieri, S., Mattia, M., Salerno, G., 2013. Insights into magma and fluid transfer at Mount Etna by a multiparametric approach: A model of the events leading to the 2011 eruptive cycle. J. Geophys. Res. Solid Earth 118, 7, 3519-3539. https://doi.org/10.1002/jgrb.50248

Pezzo, G., Palano, M., Tolomei, C., De Gori, P., Calcaterra, S., Gambino, P., Chiarabba, C., 2020. Flank sliding: A valve and a sentinel for paroxysmal eruptions and magma ascent at Mount Etna, Italy. Geology 48, 1077-1082. https://doi.org/10.1130/G47656.1

Pompilio, M., Bertagnini, A., Del Carlo, P., Di Roberto, A., 2017. Magma dynamics within a basaltic conduit revealed by textural and compositional features of erupted ash: the December 2015 Mt. Etna paroxysms. Sci. Rep. 7, 4805. https://doi.org/10.1038/s41598-017-05065-x

Ruprecht, P., Wörner, G., 2007. Variable regimes in magma systems documented in plagioclase zoning patterns: El Misti stratovolcano and Andahua monogenetic cones. J. Volcanol. Geotherm. Res. 165, 3-4, 142-162. https://doi.org/10.1016/j.jvolgeores.2007.06.002

Saunders, K., Blundy, J., Dohmen, R., Cashman, K., 2012. Linking petrology and seismology at an active volcano. Science 336, 1023-1027. http://doi.org/10.1126/science.1220066

Sciotto, M., Cannata, A., Privitera, E., Gresta, S., Di Grazia, G., 2011. Seismo-acoustic investigations of paroxysmal activity at Mt. Etna volcano: New insights into 16 November 2006. J. Geophys. Res. Solid Earth 116, B9. https://doi.org/10.1029/2010JB008138

Spampinato, L., Sciotto, M., Cannata, A., Cannavò, F., La Spina, A., Palano, M., Salerno, G., Privitera, E., Caltabiano, T., 2015. Multi-parametric study of the February-April 2013 paroxysmal phase of Mt. Etna New South-East crater. Geochem. Geophys. Geosyst. 16, 1932–1949. https://doi:10.1002/2015GC005795

Spampinato, S., Langer, H., Messina, A. et al. 2019. Short-term detection of volcanic unrest at Mt. Etna by means of a multi-station warning system. Sci. Rep. 9, 6506. https://doi.org/10.1038/s41598-019-42930-3

Spina, L., Cannata, A., Privitera, E., Vergniolle, S., Ferlito, C., Gresta, S., Montalto, P., Sciotto, M., 2015. Insights into Mt. Etna's shallow plumbing system from the analysis of infrasound signals, August 2007–December 2009. Pure Appl. Geophys. 172, 473-490. https://doi.org/10.1007/s00024-014-0884-x

Shea, T., Lynn, K.J., Garcia, M.O., 2015a. Cracking the olivine zoning code: Distinguishing between crystal growth and diffusion. Geology 43, 935-938.

Shea, T., Costa, F., Krimer, D., Hammer, J.E, 2015b. Accuracy of timescales retrieved from diffusion modeling in olivine: a 3D perspective. Am. Mineral. 100, 2026-2042. https://doi.org/10.2138/am-2015-5163

Stewart, M.L., Fowler, A.D., 2001. The nature and occurrence of discrete zoning in plagioclase from recently erupted andesitic volcanic rocks, Montserrat. J. Volcanol. Geotherm. Res. 106, 243-253. https://doi.org/10.1016/S0377-0273(00)00240-7

Streck, M. J., 2008. Mineral textures and zoning as evidence for open system processes. Rev. Mineral. Geochem. 69, 595-622. https://doi.org/10.2138/rmg.2008.69.15

Tepley, F.J., Davidson, J.P., Clynne, M.A., 1999. Magmatic interactions as recorded in plagioclase phenocrysts of Chaos Crags, Lassen Volcanic Center, California. J. Petrol. 40, 787–806. https://doi.org/10.1093/petroj/40.5.787

Tsuchiyama, A., 1985. Dissolution kinetics of plagioclase in the melt of the system diopside-albite-anorthite, and origin of dusty plagioclase in andesites. Contrib. Mineral. Petrol. 89, 1–16. https://doi.org/10.1007/BF01177585

Ubide, T., Kamber, B., 2018. Volcanic crystals as time capsules of eruption history. Nat. Comm. 9, 326. https://doi.org/10.1038/s41467-017-02274-w

Viccaro, M., Giacomoni, P.P., Ferlito, C., Cristofolini, R., 2010. Dynamics of magma supply at Mt. Etna volcano (Southern Italy) as revealed by textural and compositional features of plagioclase phenocrysts. Lithos 116, 77-91. https://doi.org/10.1016/j.lithos.2009.12.012

Viccaro, M., Giuffrida, M., Nicotra, E., Ozerov, A.Yu., 2012. Magma storage, ascent and recharge history prior to the 1991 eruption at Avachinsky Volcano, Kamchatka, Russia: inferences on the plumbing system geometry. Lithos 140-141, 11-24. https://doi.org/10.1016/j.lithos.2012.01.019

Viccaro, M., Garozzo, I., Cannata, A., Di Grazia, G., Gresta, S., 2014. Gas burst vs. gas-rich magma recharge: A multidisciplinary study to reveal factors controlling duration of the recent paroxysmal eruptions at Mt. Etna. J. Volcanol. Geotherm. Res. 278–279, 1–13. https://doi.org/10.1016/j.jvolgeores.2014.04.001

Viccaro, M., Barca, D., Bohrson, W.A., D'Oriano, C., Giuffrida, M., Nicotra, E., Pitcher, B.W., 2016a. Crystal residence times from trace element zoning in plagioclase reveal changes in magma transfer dynamics at Mt. Etna during the last 400 years. Lithos 248-251, 309-323, https://doi.org/10.1016/j.lithos.2016.02.004

Viccaro, M., Giuffrida, M., Nicotra, E., Cristofolini, R., 2016b. Timescales of magma storage and migration recorded by olivine crystals in basalts of the March-April 2010 eruption at

Eyjafjallajökull volcano, Iceland. Am. Mineral. 101, 222–230. https://doi.org/10.2138/am-2016-5365

Viccaro, M., Zuccarello, F., Cannata, A., Palano, M., Gresta, S., 2016c. How a complex basaltic volcanic system works: Constraints from integrating seismic, geodetic, and petrological data at Mount Etna volcano during the July–August 2014 eruption. J. Geophys. Res. Solid Earth 121, 5659–5678. https://doi.org/10.1002/2016JB013164

Viccaro, M., Giuffrida, M., Zuccarello, F., Scandura, M., Palano, M., Gresta, S., 2019. Violent paroxysmal activity drives self-feeding magma replenishment at Mt. Etna. Sci. Rep. 9, 6717. https://doi.org/10.1038/s41598-019-43211-9

Viccaro, M., Cannata, A., Cannavò, F., De Rosa, R., Giuffrida, M., Nicotra, E., Petrelli, M., Sacco, G., 2021. Shallow conduit dynamics fuel the unexpected paroxysms of Stromboli volcano during the summer 2019. Sci. Rep. 11, 266. https://doi.org/10.1038/s41598-020-79558-7

Wallace, G.S., Bergantz, G.W., 2002. Wavelet-based correlation (WBC) of zoned crystal populations and magma mixing. Earth Plan. Sci. Lett. 202, 133-145. https://doi.org/10.1016/S0012-821X(02)00762-8

Wallace, G.S., Bergantz, G.W., 2003. Constraints on mingling of crystal populations from off-center zoning profiles: A statistical approach. Am. Mineral. 89, 64-73.

Watson, L.M., Johnson, J.B., Sciotto, M., Cannata, A., 2020. Changes in crater geometry revealed by inversion of harmonic infrasound observations: 24 December 2018 eruption of Mount Etna, Italy. Geophys. Res. Lett. 47, e2020GL088077. https://doi.org/10.1029/2020GL088077

Zhang, Y., J. Cherniak, D.J., 2010. Diffusion in minerals and melts: Introduction. Rev. Mineral. Geochem. 72, 1–4. https://doi.org/10.2138/rmg.2010.72.1

Zuccarello, F., Schiavi, F., Viccaro, M., 2021. Magma dehydration controls the energy of recent eruptions at Mt. Etna volcano. Terra Nova 33, 4. https://doi.org/10.1111/ter.12527

Figure captions

Figure 1. (a): Digital elevation model of Mt. Etna volcano, with locations of seismic (dark square) and infrasound (open circle) stations, and lava flows relative to the eruptive episodes of May 30 – June 5, 2019, July 18-20, 2019 and July 27-28, 2019 [lava flows are taken from the INGV-OE Internal Report (2019a; 2019e; 2020c)]. The insert shows a magnification of the summit area with the active craters (VOR: Voragine, BN: Bocca Nuova, NEC: North East Crater, SEC: South East Crater, NSEC: New South East Crater) and the lava flow emitted from the scoria cone built inside the VOR crater during the Strombolian activity started since September 2019; (b): Sketch showing the eruptive activity for each summit crater over the time (from March 1, 2019 to June 1, 2020).

Figure 2. Representative core-to-rim compositional profiles for An mol% (black diamond) and FeO wt.% (open square) measured on plagioclase crystals having different textures. The white line in BSE images represents the compositional traverse measured by SEM-EDS/WDS, while the dashed yellow line indicates the boundary of CS textures. Error bars for An mol% are within the symbols.

Figure 3. Frequency diagrams of the observed plagioclase textural types. In each diagram, histograms indicate the relative percentage of textures for samples collected during the July 27-28, 2019 eruption at NSEC and the November 2019 – January 2020 activity at VOR. OZp: core-to-rim oscillatory zoning, CS: coarse-sieve textured cores, D: dissolved cores, ST: sieve-textures, CS+ST: complex textural feature given by the sequence of sieve textures at the core and rim.

Figure 4. Representative compositional profiles (Fo mol%) of olivine crystals erupted between July 2019 and January 2020, with indication of the corresponding zoning type. N: simple normal zoning; R: simple reverse zoning; R+N: complex zoning type given by the sequence of reverse plus normal zoning; N+R: complex zoning type given by the sequence of reverse plus normal zoning.
The yellow line on BSE images refers to the compositional traverse measured by SEM-EDS/WDS.

Figure 5. Frequency of forsterite compositions (Fo mol%) measured at the core of olivine crystals and relative percentage of zoning types (reported in inserts) for each sample collected during the July 27-28, 2019 eruption at NSEC and the November 2019 – January 2020 activity at VOR. OZ: core-to-rim homogeneous Fo concentration, N: simple normal zoning; R: simple reverse zoning; R+N: complex zoning type given by the sequence of reverse plus normal zoning; N+R: complex zoning type given by the sequence of reverse plus normal zoning.

Figure 6. Sketch summarizing the main eruptive activities at the summit craters during the investigated time period (a), evolution in time of location of the volcanic tremor source centroid (b, c, d) and corresponding amplitude (e), and map (f), sections (g, h) and 3D view (i) of Mt. Etna, showing the location of the volcanic tremor source centroid. The color of the dots in (f-i) depends on the time (see b-e).

Figure 7. Sketch summarizing the main eruptive activities at the summit craters during the investigated time period (a), reduced amplitude (b) and daily number of infrasound events radiated by the four summit crater areas (c-f). The red, black, green and blue dots in (b) indicate the reduced amplitudes of the events generated by BN, VOR, SEC/NSEC and NEC, respectively.

Figure 8. a) Schematic cartoon of Mt. Etna plumbing system illustrating the magmatic environments (M*i*) and related pressure and depth ranges; b) Timeline of the 2019-2020 volcanic activity at the three craters NSEC (in blue), NEC (green) and VOR (red) in relation with key petrological and geophysical signals detected in this study. The temporal variation from March 1, 2019 to February 1, 2020 of the reduced root-mean-square (RMS) tremor amplitude (upper panel) is shown together with the main magmatic intrusive episodes (lower panel) involving the compositionally-distinct environments. Coloured rectangles refer to the time of intrusion in a given environment as determined from olivine diffusion. Uncertainties on time calculations are expressed by horizontal black lines departing from a single rectangle. The rectangle size is proportional to the time interval over which magmatic intrusions are recorded. The rectangle colour indicates the eruption of reference. Vertical dotted lines in the lower panel indicate the date of sampling.

Figure 9. Examples of Fe-Mg diffusion profiles obtained on olivine crystals erupted between July 2019 and January 2020. For each modeled profile are shown the initial concentration (dashed blue line), the best fit diffusion curve (red line), calculated timescales with relative uncertainties, and the magmatic environments (M*i*) involved. The yellow line on BSE images indicates the SEM-EDS/WDS compositional traverse. Note that the initial profile for any single olivine has been fixed by considering the chemical heterogeneity of the environments in which the olivine grew, in a way that the maximum concentration in the step-like profile coincides with the highest Fo values within the compositional range associated to the host environment.

Table 1. Diffusion modeling results for olivine crystals erupted during2019-2020 at Mt. Etna. Temperature, pressure and oxygen fugacity used for the modeling are also shown in the table. Timescales (days) and relative uncertainties (±σ) were calculated for distinct zoned portions of an olivine crystal (n: normal; r: reverse), indicating a given connection between two magmatic environments (M_i).

Date	Crystal	T (°C)	P (MPa)	fO_2 (bars)	M_i	Δt ± σ
Jul 27, 2020	ol1_ET2	1130	260	$10^{-8.92}$	M0-M1a (n)	37 ± 11
	ol2_ET2	1130	140	$10^{-8.92}$	M1b-M1a (r)	41 ± 12
	ol1_ET4	1130	140	$10^{-8.92}$	M1b-M1a (r)	36 ± 11
	ol3_ET4	1130	140	$10^{-8.92}$	M1b-M1a (r)	33 ± 10
	ol1_ET3	1158	140	$10^{-8.49}$	M1b-M0 (r)	29 ± 8
	ol2_ET3	1158	140	$10^{-8.49}$	M1b-M0 (r)	28 ± 8
	ol1_SEZ2	1130	140	$10^{-8.92}$	M1b-M1a (r)	33 ± 10
Nov 4, 2020	ol1_ET2	1108	30	$10^{-9.28}$	M2-M1b (r)	137 ± 42
	ol3_ET2	1080	30	$10^{-9.65}$	M1b-M2 (n)	180 ± 57
	ol8_ET2	1080	30	$10^{-9.65}$	M1a-M2 (n)	132 ± 42
	ol9_ET2	1080	30	$10^{-9.65}$	M1a-M2 (n)	12 ± 4
Dec 19, 2019	ol1_ET400	1080	30	$10^{-9.65}$	M0-M2 (n)	255 ± 41
	ol5_ET400	1158	260	$10^{-8.49}$	M1a-M0 (r)	51 ± 15
	ol3_ET100	1080	30	$10^{-9.65}$	M2b-M2 (r)	3 ± 1
	ol4_ET100	1080	30	$10^{-9.65}$	M1b-M2 (n)	36 ± 11
Jan 24, 2020	ol1_ET1	1158	260	$10^{-8.49}$	M1a-M0 (r)	23 ± 3
	ol1_ET20	1158	260	$10^{-8.49}$	M1a-M0 (r)	30 ± 9
	ol2_ET2	1080	30	$10^{-9.65}$	M1b-M2 (n)	2 ± 1
	ol3_ET2	1080	20	$10^{-9.65}$	M2b-M2 (r)	11 ± 3
	ol4_ET2	1108	30	$10^{-9.28}$	M2-M1b (r)	4 ± 1

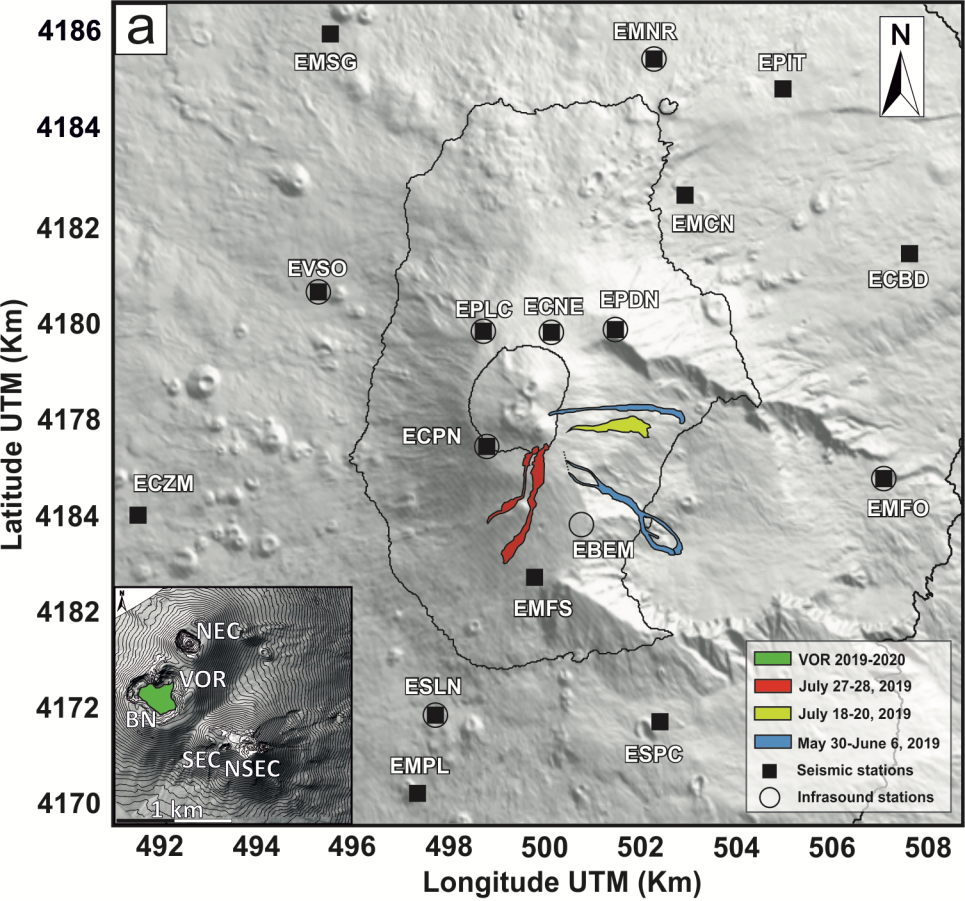
a
EMSG
EMNR
EPIT
N
EMCN
EVSO
ECBD
EPLC
ECNE
EPDN
ECPN
ECZM
EMFO
EBEM
EMFS
ESLN
EMPL
ESPC
NEC
VOR
BN
SEC
NSEC
1 km
VOR 2019-2020
July 27-28, 2019
July 18-20, 2019
May 30-June 6, 2019
Seismic stations
Infrasound stations
Latitude UTM (Km)
4186
4184
4182
4180
4178
4184
4182
4172
4170
492
494
496
498
500
502
504
506
508
Longitude UTM (Km)

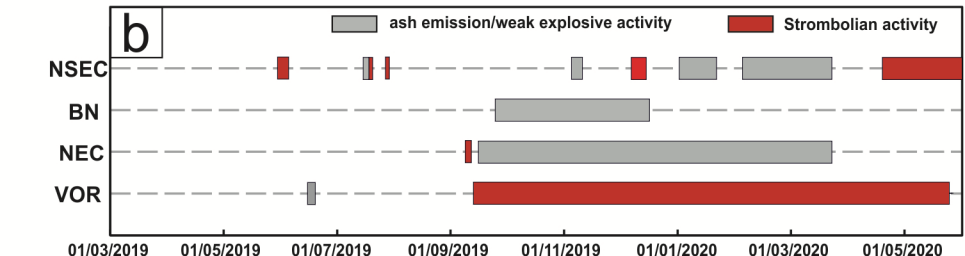
b
ash emission/weak explosive activity
Strombolian activity
NSEC
BN
NEC
VOR
01/03/2019
01/05/2019
01/07/2019
01/09/2019
01/11/2019
01/01/2020
01/03/2020
01/05/2020

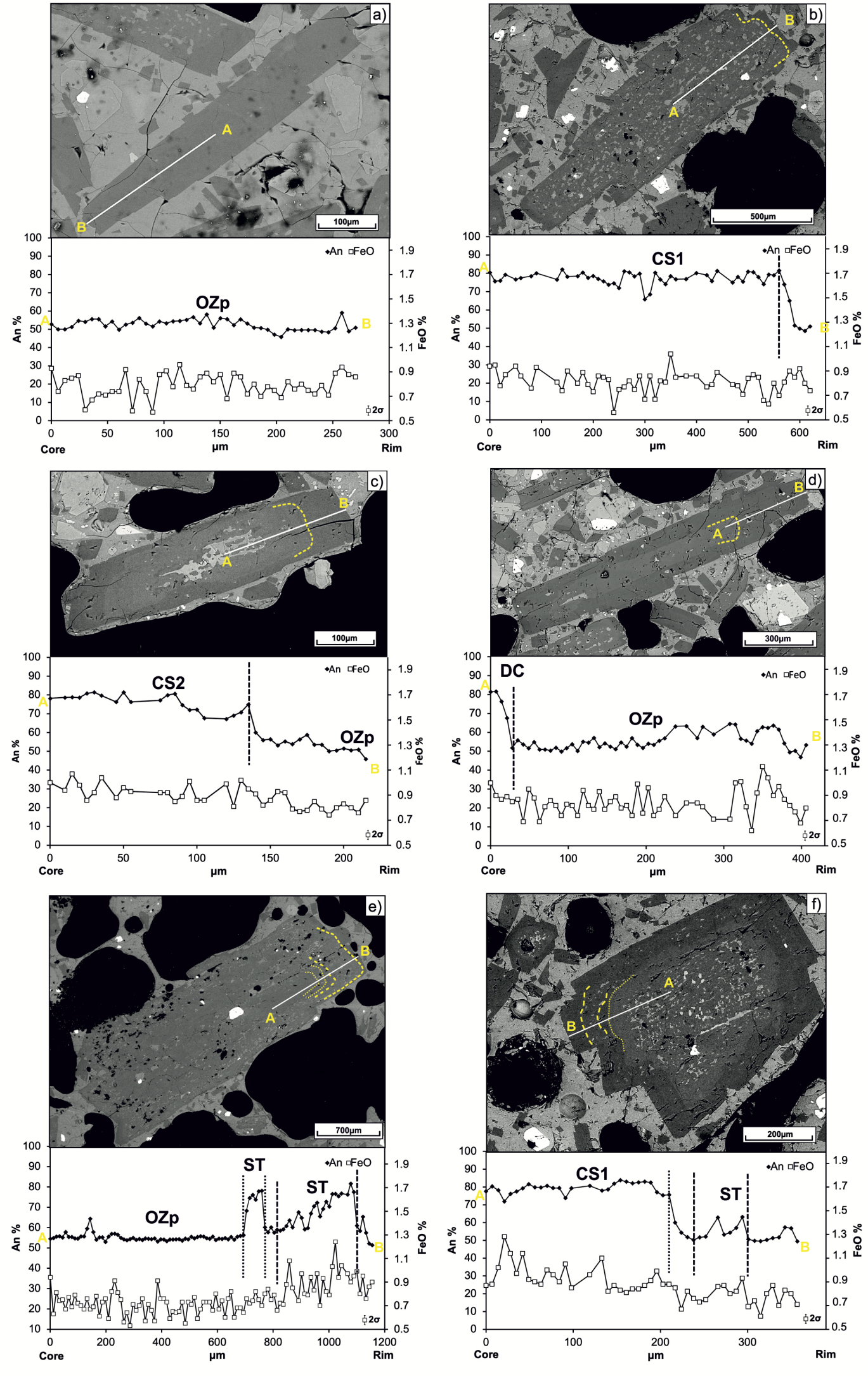
a)
100µm
A
B
OZp
An %
FeO %
Core
µm
Rim
2σ
b)
500µm
CS1
c)
100µm
CS2
OZp
d)
300µm
DC
OZp
e)
700µm
ST
ST
OZp
f)
200µm
CS1
ST

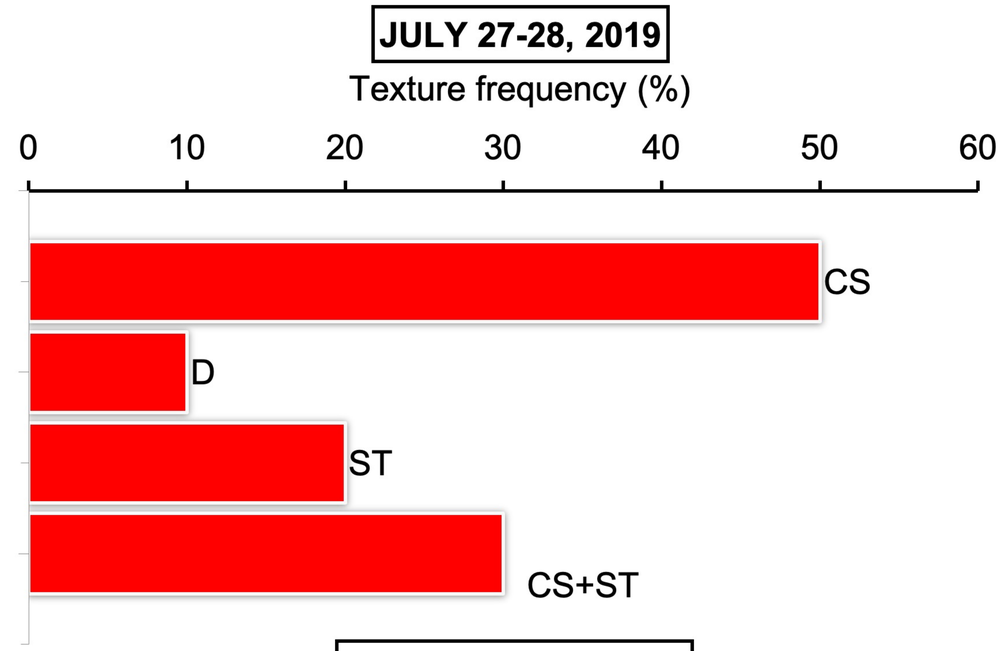
JULY 27-28, 2019
Texture frequency (%)
0
10
20
30
40
50
60
CS
D
ST
CS+ST

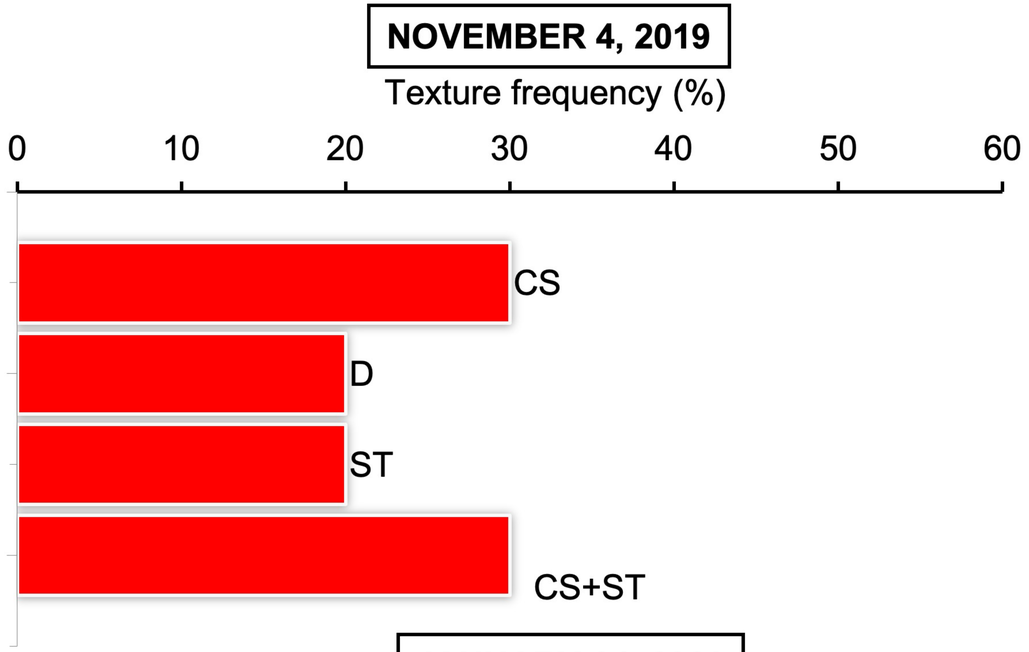
NOVEMBER 4, 2019
Texture frequency (%)
0
10
20
30
40
50
60
CS
D
ST
CS+ST

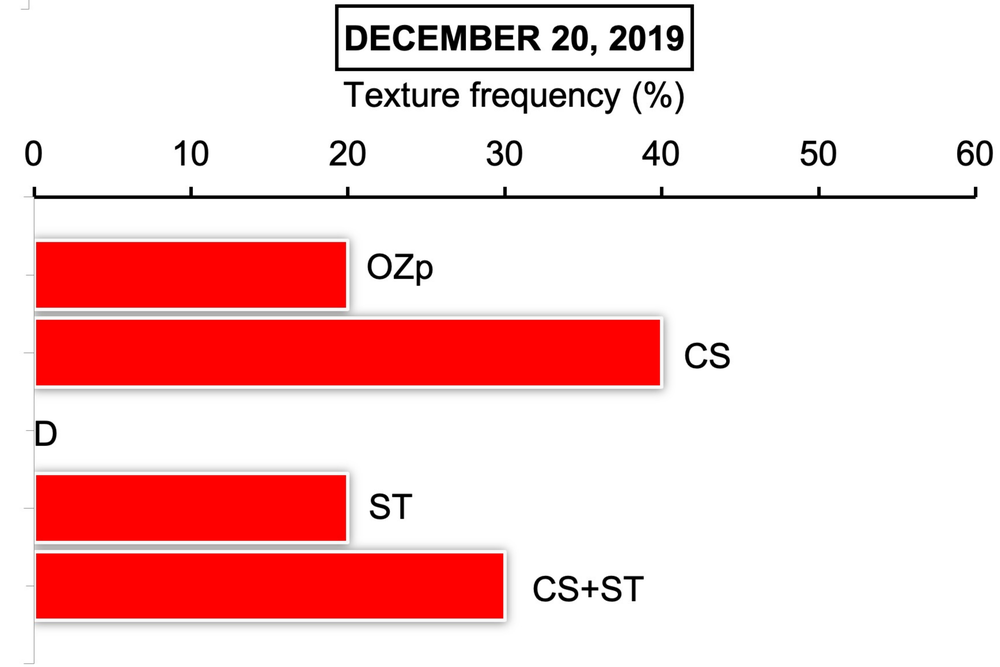
DECEMBER 20, 2019
Texture frequency (%)
0
10
20
30
40
50
60
OZp
CS
D
ST
CS+ST

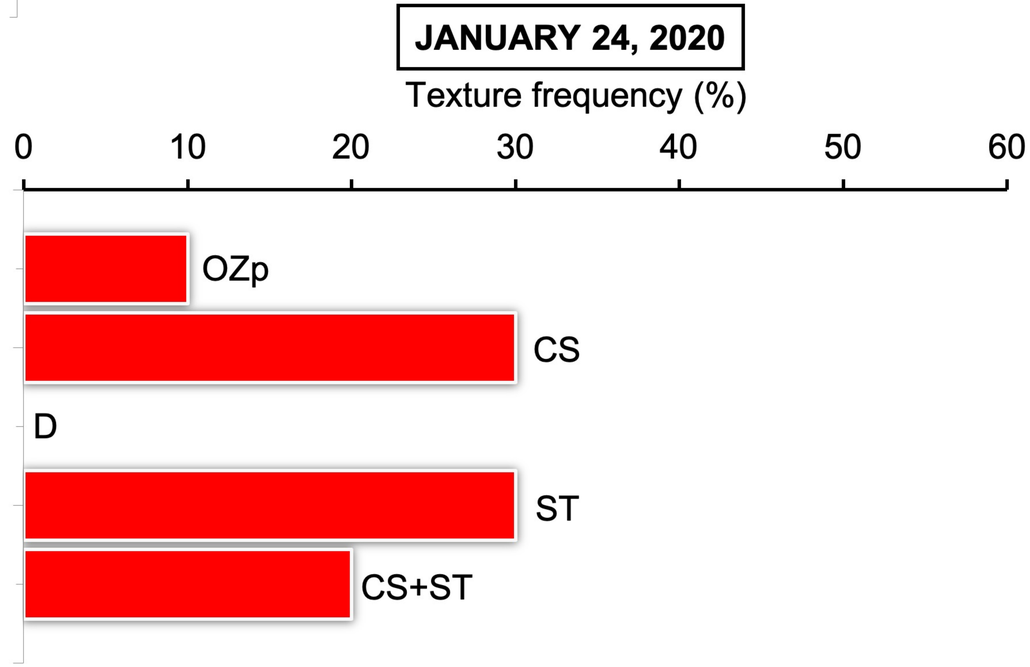
JANUARY 24, 2020
Texture frequency (%)
0
10
20
30
40
50
60
OZp
CS
D
ST
CS+ST

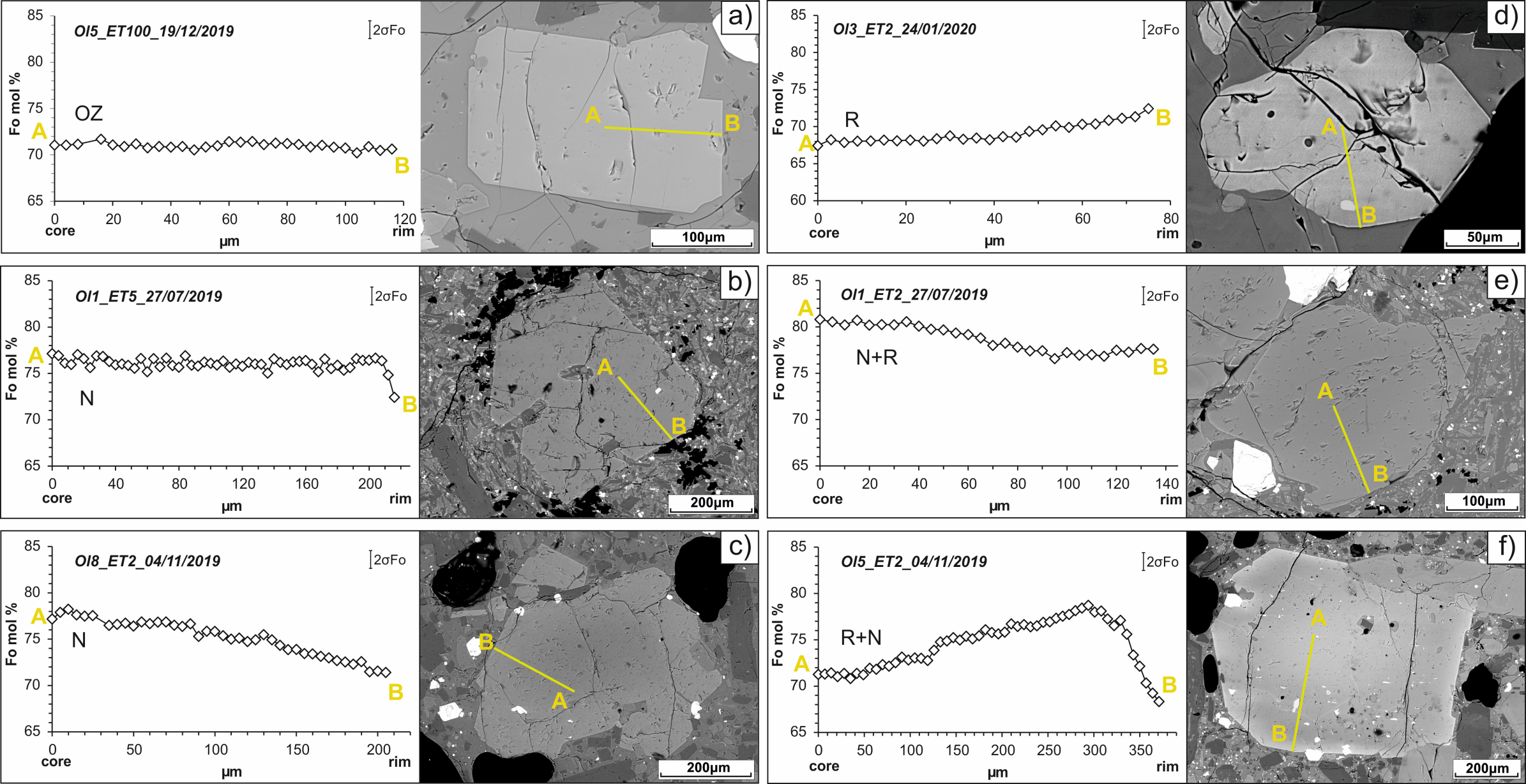
Ol5_ET100_19/12/2019
2σFo
Fo mol %
OZ
A
B
core
rim
µm
a)
100µm
Ol3_ET2_24/01/2020
R
d)
50µm
Ol1_ET5_27/07/2019
N
b)
200µm
Ol1_ET2_27/07/2019
N+R
e)
100µm
Ol8_ET2_04/11/2019
c)
200µm
Ol5_ET2_04/11/2019
R+N
f)
200µm

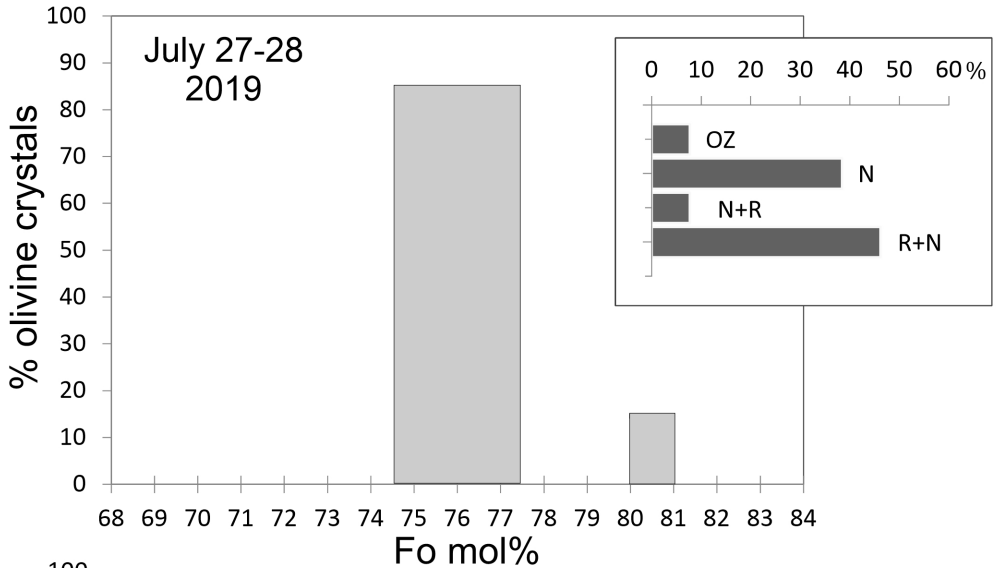
July 27-28
2019
% olivine crystals
Fo mol%
0 10 20 30 40 50 60%
OZ
N
N+R
R+N

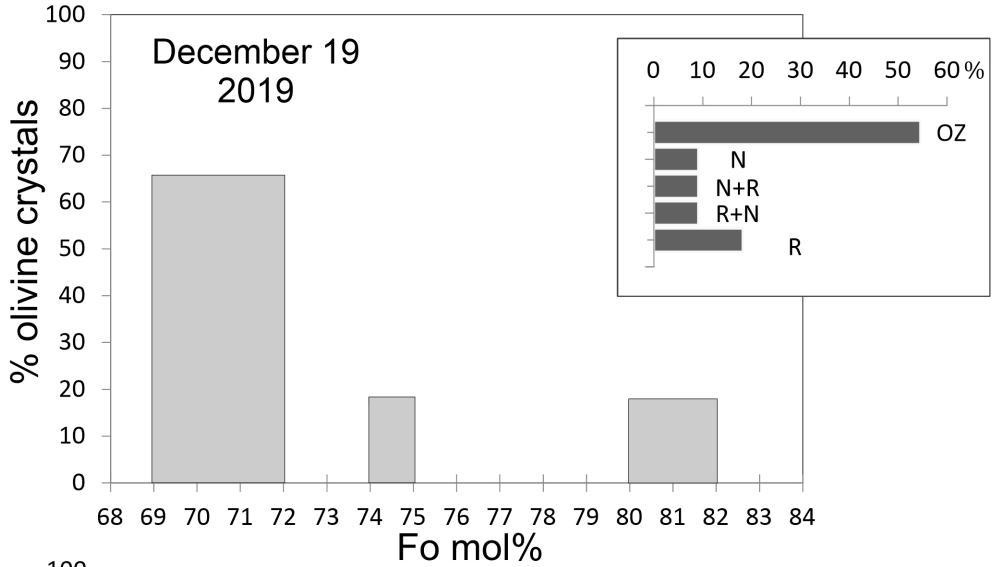
December 19
2019
% olivine crystals
Fo mol%
0 10 20 30 40 50 60%
OZ
N
N+R
R+N
R

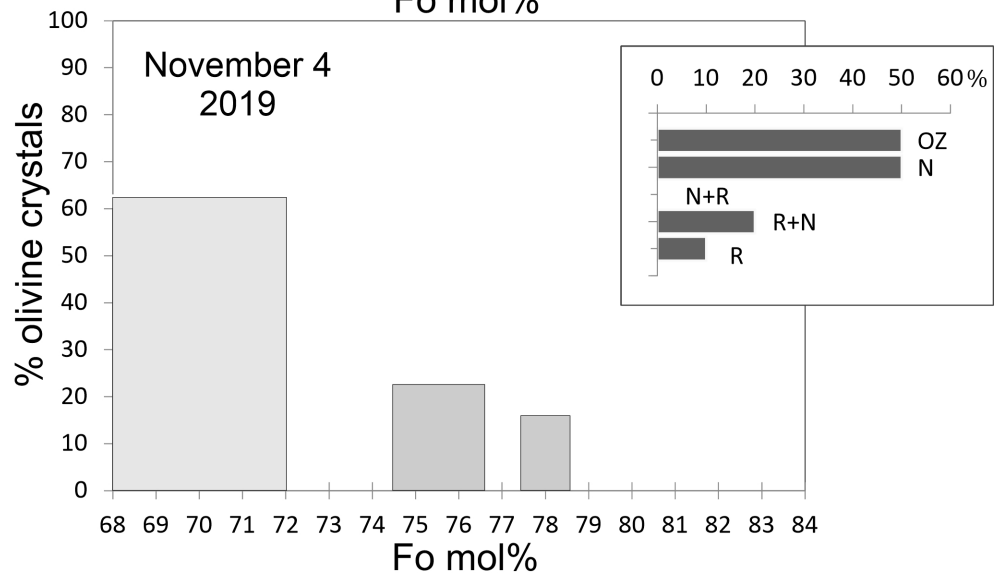
November 4
2019
% olivine crystals
Fo mol%
0 10 20 30 40 50 60%
OZ
N
N+R
R+N
R

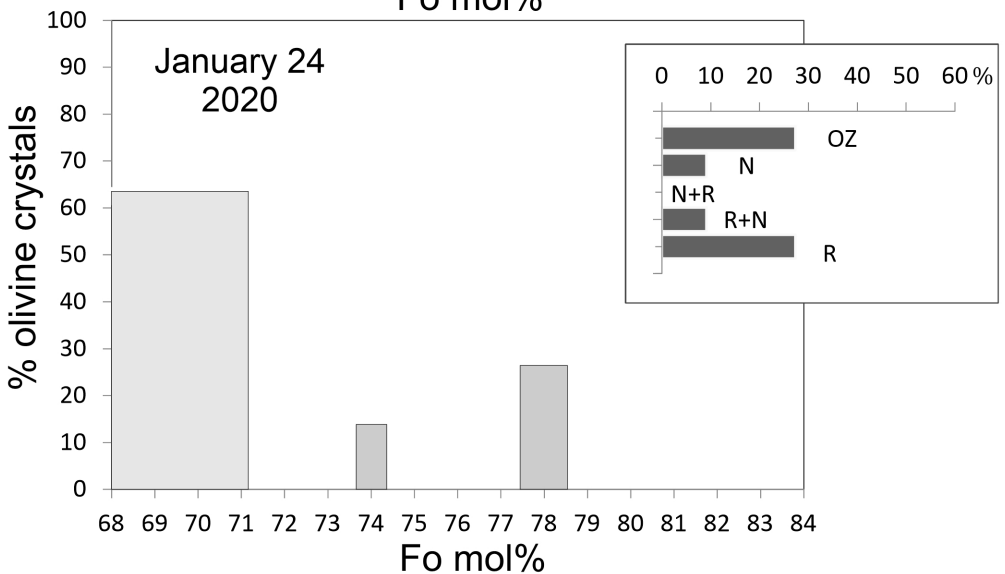
January 24
2020
% olivine crystals
Fo mol%
0 10 20 30 40 50 60%
OZ
N
N+R
R+N
R

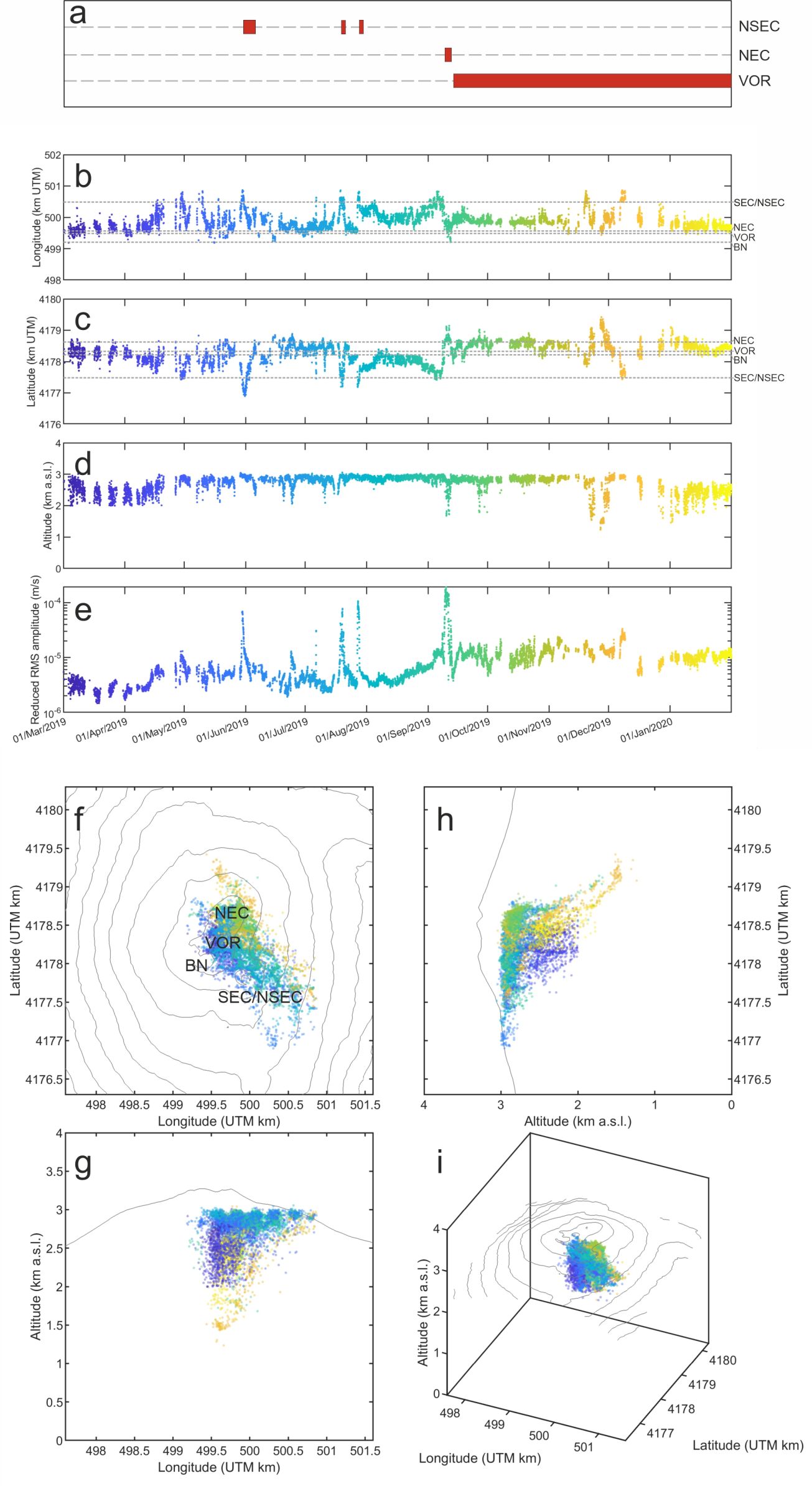
a
NSEC
NEC
VOR
b
Longitude (km UTM)
SEC/NSEC
NEC
VOR
BN
c
Latitude (km UTM)
NEC
VOR
BN
SEC/NSEC
d
Altitude (km a.s.l.)
e
Reduced RMS amplitude (m/s)
01/Mar/2019
01/Apr/2019
01/May/2019
01/Jun/2019
01/Jul/2019
01/Aug/2019
01/Sep/2019
01/Oct/2019
01/Nov/2019
01/Dec/2019
01/Jan/2020
f
NEC
VOR
BN
SEC/NSEC
Latitude (UTM km)
Longitude (UTM km)
h
Altitude (km a.s.l.)
Latitude (UTM km)
g
Altitude (km a.s.l.)
Longitude (UTM km)
i
Altitude (km a.s.l.)
Longitude (UTM km)
Latitude (UTM km)

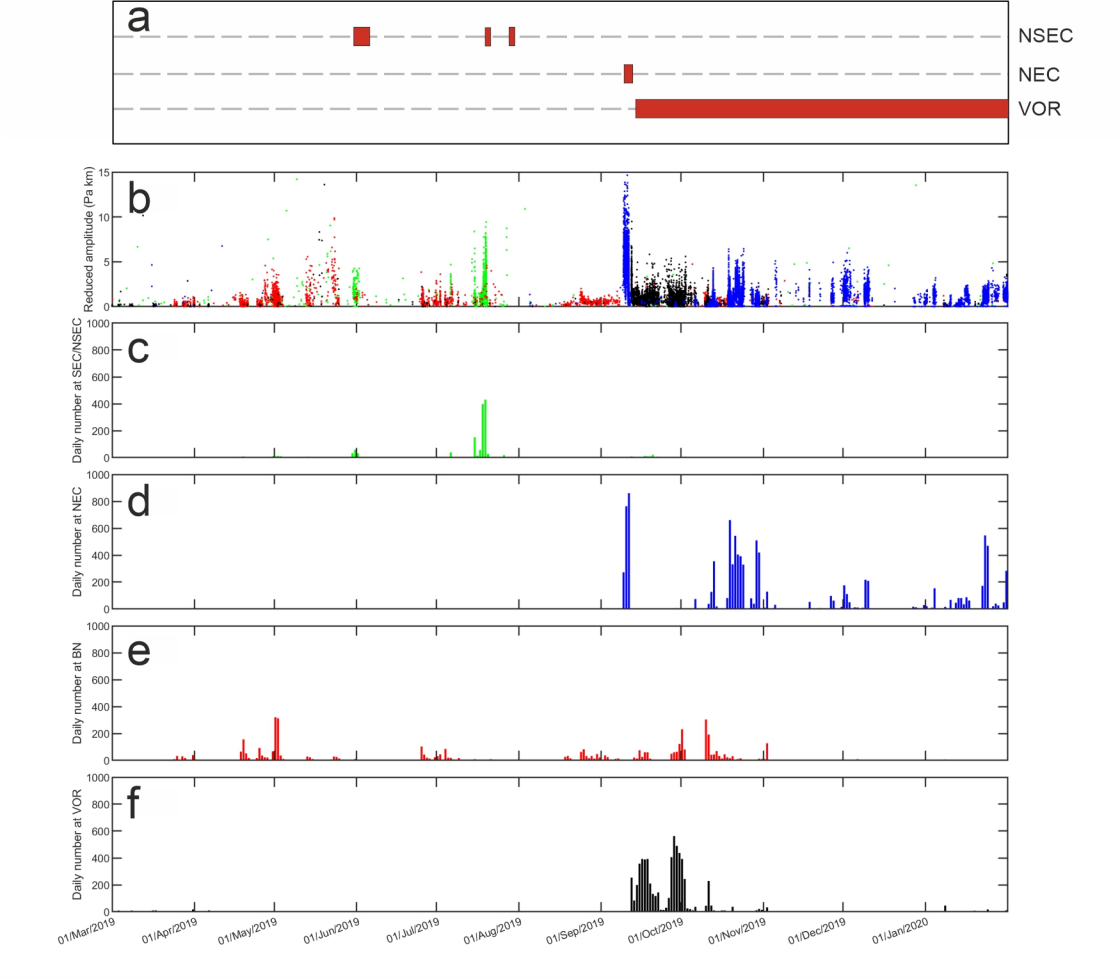
a
NSEC
NEC
VOR
b
Reduced amplitude (Pa km)
c
Daily number at SEC/NSEC
d
Daily number at NEC
e
Daily number at BN
f
Daily number at VOR
01/Mar/2019
01/Apr/2019
01/May/2019
01/Jun/2019
01/Jul/2019
01/Aug/2019
01/Sep/2019
01/Oct/2019
01/Nov/2019
01/Dec/2019
01/Jan/2020

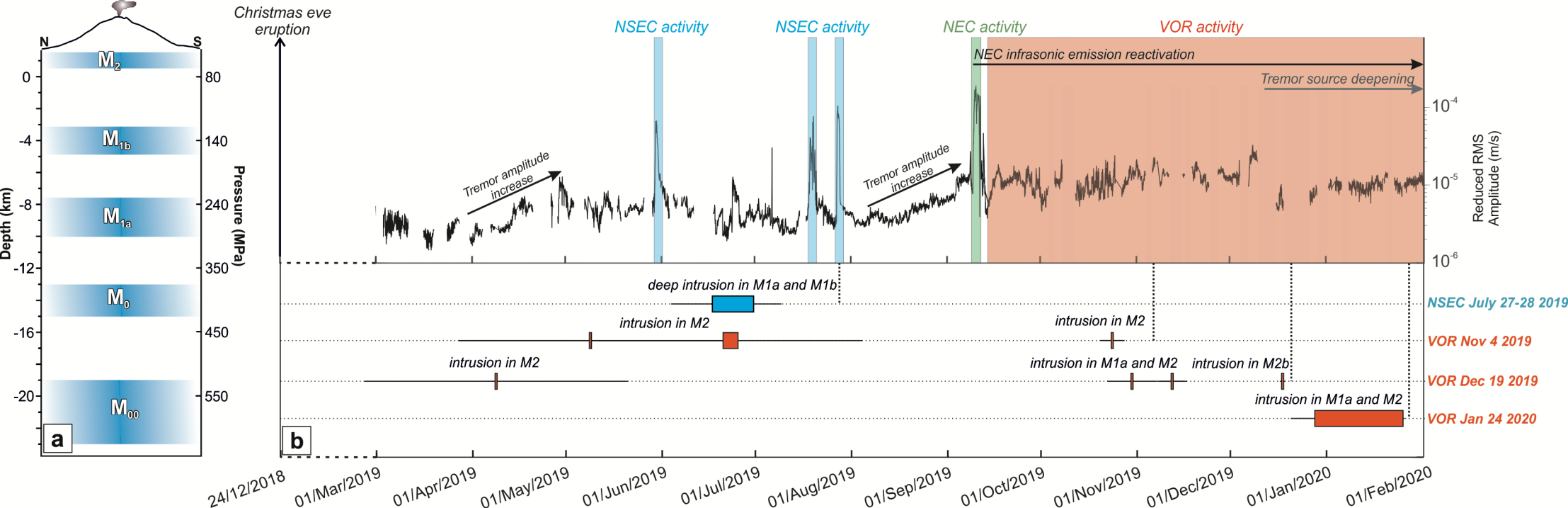
N
S
M_2
M_{1b}
M_{1a}
M_0
M_{00}
Depth (km)
Pressure (MPa)
a
b
Christmas eve eruption
NSEC activity
NSEC activity
NEC activity
VOR activity
NEC infrasonic emission reactivation
Tremor source deepening
Tremor amplitude increase
Tremor amplitude increase
Reduced RMS Amplitude (m/s)
deep intrusion in M1a and M1b
intrusion in M2
intrusion in M2
intrusion in M2
intrusion in M1a and M2
intrusion in M2b
intrusion in M1a and M2
NSEC July 27-28 2019
VOR Nov 4 2019
VOR Dec 19 2019
VOR Jan 24 2020
24/12/2018
01/Mar/2019
01/Apr/2019
01/May/2019
01/Jun/2019
01/Jul/2019
01/Aug/2019
01/Sep/2019
01/Oct/2019
01/Nov/2019
01/Dec/2019
01/Jan/2020
01/Feb/2020

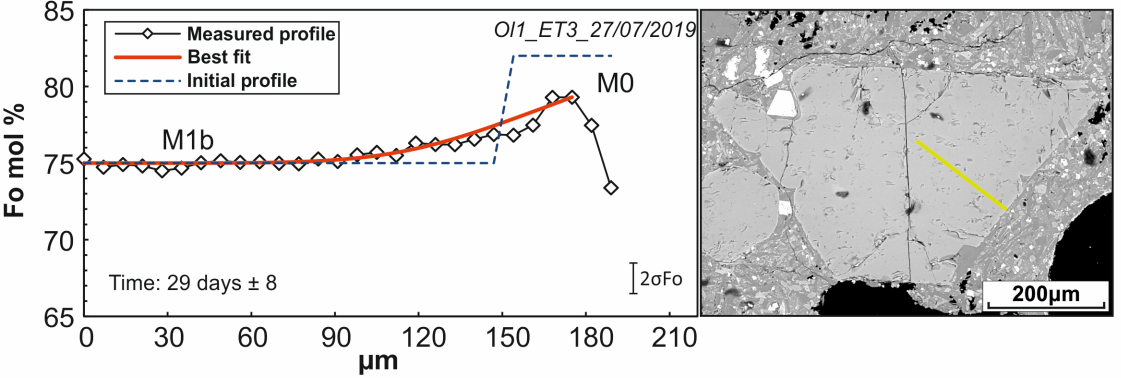
Measured profile
Best fit
Initial profile
Ol1_ET3_27/07/2019
M0
M1b
Time: 29 days ± 8
2σFo
200µm
Fo mol %
µm

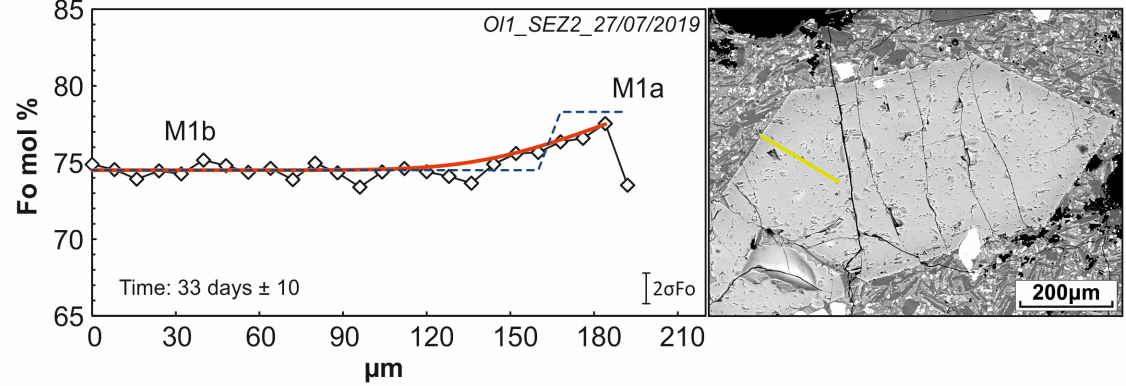
Ol1_SEZ2_27/07/2019
M1a
M1b
Time: 33 days ± 10
2σFo
200µm
Fo mol %
µm

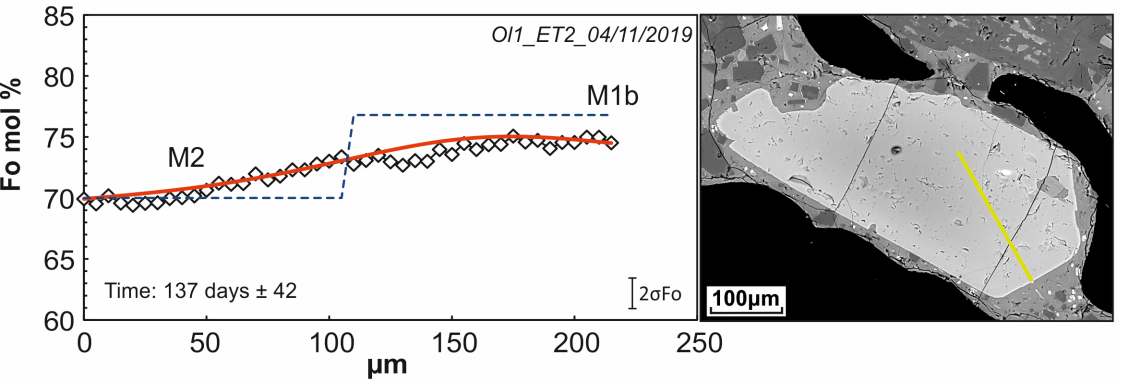
Ol1_ET2_04/11/2019
M1b
M2
Time: 137 days ± 42
2σFo
100µm
Fo mol %
µm

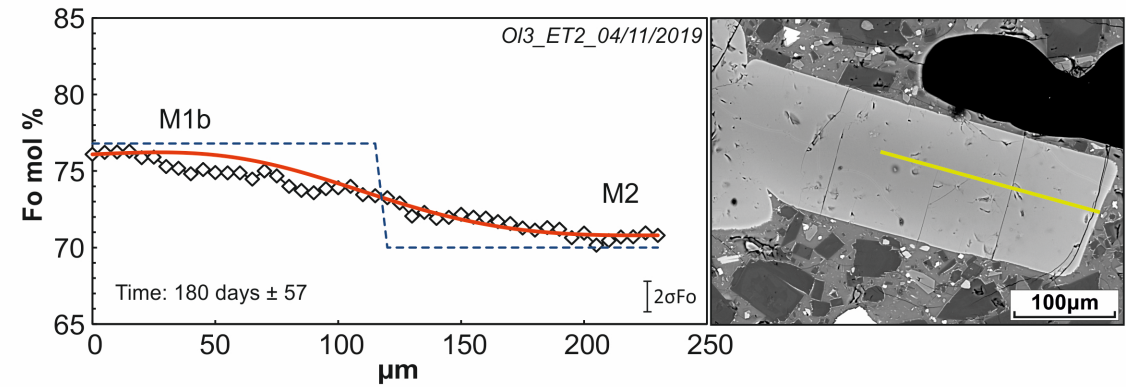
Ol3_ET2_04/11/2019
M1b
M2
Time: 180 days ± 57
2σFo
100µm
Fo mol %
µm

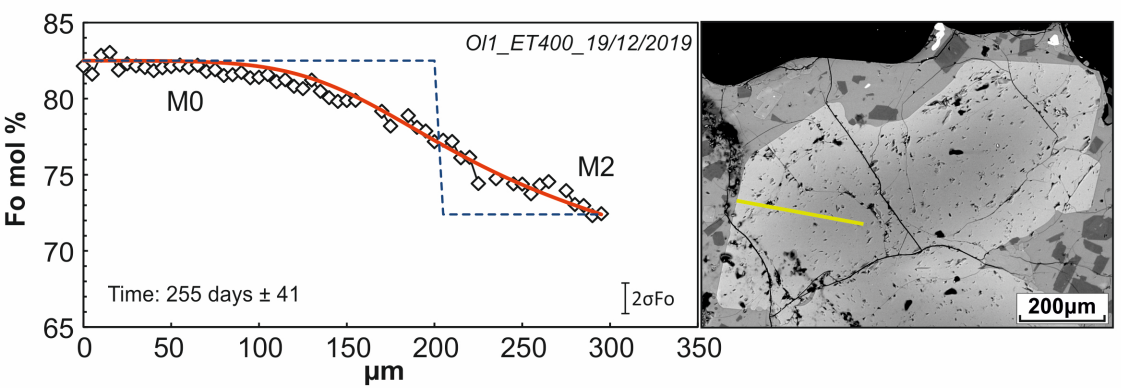
Ol1_ET400_19/12/2019
M0
M2
Time: 255 days ± 41
2σFo
200µm
Fo mol %
µm

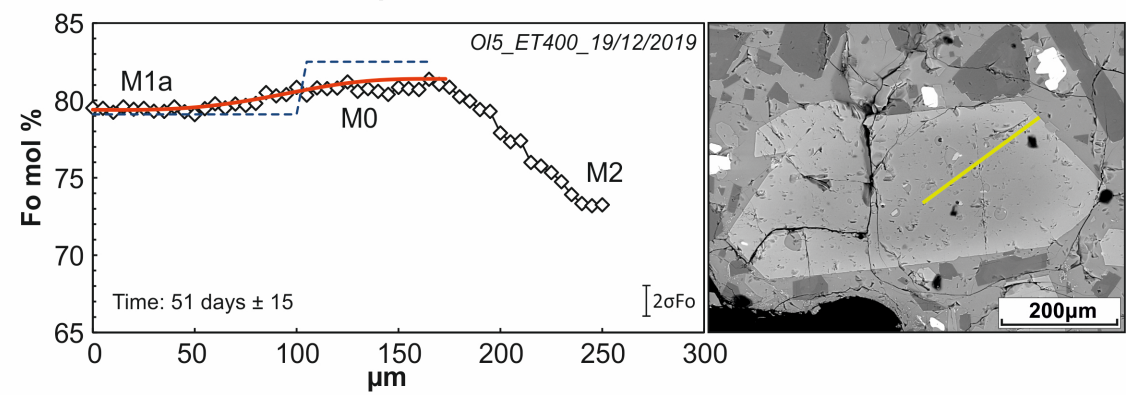
Ol5_ET400_19/12/2019
M1a
M0
M2
Time: 51 days ± 15
2σFo
200µm
Fo mol %
µm

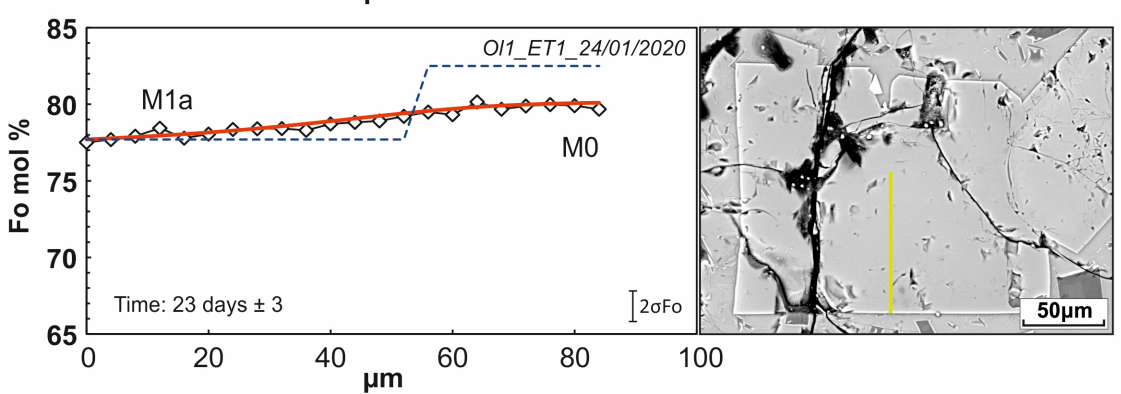
Ol1_ET1_24/01/2020
M1a
M0
Time: 23 days ± 3
2σFo
50µm
Fo mol %
µm

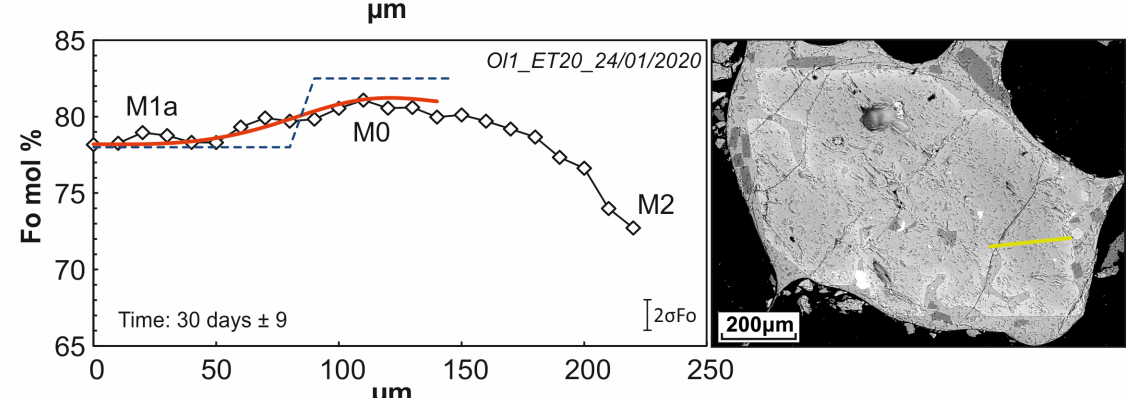
Ol1_ET20_24/01/2020
M1a
M0
M2
Time: 30 days ± 9
2σFo
200µm
Fo mol %
µm